Universiteit Utrecht

Masters Experimental Physics

Exploring open charmed hadron production in heavy-ion collisions within the *Trajectum* theoretical framework.

Master Thesis

Teun de Theije BSc.

Supervisors:

Dr. Alessandro Grelli
Utrecht University

Dr. R.J.M. Snellings
Utrecht University

Olaf Massen MSc.
Utrecht University

February 12, 2024

Abstract

This paper presents the study of open charmed hadron production in ultra-relativistic Pb-Pb collisions at a center of mass energy of $\sqrt{s_{NN}} = 5.02$ TeV, carried out within the *Trajectum* theoretical framework. Charm quarks are viewed as excellent probes of the deconfined state of matter formed in these collisions, the quark-gluon plasma (QGP). The initial conditions for the heavy-ion collision is simulated using the TRENTomodel for the transverse profile. The space-time evolution of the medium temperature and its flow velocity field are calculated through (2+1)-dimensional viscous relativistic hydrodynamics. The motion of charm quarks through the medium is treated as Brownian motion and modeled using a Langevin approach. For the subsequent formation of hadrons a hybrid hadronization method is employed, including hadronization through both fragmentation and coalescence. The fragmentation parameters are tuned based on comparison to data in a pp collision environment. The strength of the coupling between the charm quarks and the constituents of the plasma is quantified by the spatial diffusion coefficient ($2\pi TD_s$). This spatial diffusion constant is modeled using a linear temperature dependence ansatz, $2\pi TD_s = \alpha(T/T_c - 1) + \beta$. We find that smaller values for α and β are able to describe $v_2(p_{\mathrm{T}})$. However, these values give a large underestimation for the p_{T}-differential multiplicities at high transverse momentum. Whilst larger values for α and β are more suited to describe the p_{T}-differential multiplicities, but this parameterization gives an underestimation of the $v_2(p_{\mathrm{T}})$. A simultaneous description for both p_{T}-differential multiplicity and $v_2(p_{\mathrm{T}})$ remains challenging within the current framework.

Contents

1 Introduction

In an extreme high temperature and energy density environment, quantum chromodynamics (QCD) predicts the phase transition of hadronic matter to a color-deconfined state of matter called the quark-gluon plasma (QGP) [1–3]. This hot and dense state of matter comprised of deconfined quarks and gluons is believed to have permeated the early universe [4]. A remarkable feature of the QGP is that it exhibits behaviour of a near perfect fluid with a very small shear viscosity to entropy density ratio, η/s. The expansion and evolution of the plasma can be described by relativistic viscous hydrodynamics [5]. Heavy ion collider experiments at the Large Hadron Collider (LHC) [6] and the Relativistic Heavy-ion Collider (RHIC) [7] aim to characterise this hot and dense state of matter produced in heavy-ion collisions.

Heavy quarks (charm and beauty) are of particular interest for probing the hot and dense plasma. Due to their heavy mass it is possible to evaluate the charm quark production cross-sections and initial transverse momentum spectra with perturbative QCD schemes [8]. In addition, thermal production of $c\bar{c}$ pairs by the QGP medium is expected to be negligible at temperatures reached at both RHIC and LHC energies [9]. Charm quarks interact with the thermal plasma constituents through elastic and inelastic (gluon radiation) [10] QCD processes. These interactions and the in medium space-time evolution of charm quarks can be modeled using a Langevin approach. Throughout these in medium interactions the flavour of charm quarks is conserved. Therefore, since charm quarks are primarily produced in hard scattering processes before formation of the QGP [11, 12], the initially produced charm quarks experience the entire medium evolution. These aforementioned reasons make charm quarks excellent probes for the QGP.

Strong modification of the transverse momentum (p_{T}) distributions of charmed hadrons in heavy ion collisions with respect to the momentum distributions found in $p+p$ collision systems are evidence for the in-medium interactions and energy loss of charm quarks [13, 14]. Transport properties of the medium can be assessed through measurements of anisotropies in the azimuthal distribution and modification of the transverse momentum (p_{T}) distribution of charmed hadrons. Initial-state spatial anisotropies are converted by the collective dynamics of the expanding plasma into final-state particle momentum anisotropy [15]. This anisotropic flow is quantified by the Fourier expansion coefficients v_n of the emitted particles azimuthal angular distribution φ relative to the initial state symmetry plane angle Ψ_n (for the n-th harmonic) [16, 17]. Anisotropic flow is also a measure of the shear viscosity of the QGP, which is one of the key transport coefficients of the medium. However, these transport properties can not be measured directly. What is possible is to create a model which simulates heavy-ion collisions where the quantities of interest are the input parameters of the model. Such a model can then attempt to recreate observables measured in experiments, such as the measurements of anisotropic flow and the modification of transverse momentum of charmed hadrons. These measurements can then be use to constrain the model parameters and extract the physics information of interest. One of these model parameters is the charm quark spatial diffusion coefficient D_s. This spatial diffusion coefficient is directly linked to the thermalization time of charm quarks in the QGP medium $\tau_Q = (m_c/T)D_s$, where T is the medium temperature and m_c is the charm quark mass. This transport coefficient conveniently encodes the in medium interactions of the charm quark with the QGP and can also be calculated through lattice QCD .

Another interesting feature of the QGP is highlighted by Au+Au measurements by the STAR collaboration [18] of charmed baryon to meson ratios, especially $\Lambda_c^{\pm}/D^0$. At intermediate transverse momentum (2-6 GeV) this ratio shows an enhancement in heavy ion collisions with respect to the ratios given by model predictions of a $p+p$ collision from perturbative QCD calculations with charm fragmentation parameters tuned on e^+e^- and e^-p measurements [19, 20]. However, model predictions including hadronization of charm quarks through both coalescence and fragmentation are able to correctly predict this enhancement in the baryon to meson ratio [21, 22]. This suggests that charm quark

coalescence plays an important role in the hadronization of charm quarks. In this work we use the *Trajectum* model developed in Ref. [23] to simulate heavy ion collisions. *Trajectum* is a state of the art event-by-event model which simulates the QGP as a hydrodynamically expanding boost-invariant (2+1D) medium. *Trajectum* employs TRENTo initial conditions and employs a hybrid hadronization model to hadronize heavy quarks. In previous works [24], the second order hydrodynamic transport coefficients have been fixed using a Bayesian parameter analysis.
This work aims to gauge the dependence of heavy quark observables generated by *Trajectum* on both the hybrid implementation of fragmentation and coalescence, and model parameters governing the charm quark spatial diffusion coefficient. This will be done by simulating pp and Pb-Pb collisions at a center-of-mass energy of $\sqrt{s_{NN}} = 5.02$ TeV, whilst varying model parameters. These simulation results will be compared to anisotropic flow and p_{T}-differential multiplicity measurements by the ALICE collaboration to try and constrain model parameters.

In this work, firstly a short summary of the relevant theoretical background for the evolution of the QGP and the evolution of heavy quarks within the medium and their subsequent hadronization will be given. This is followed by an explanation of the *Trajectum* framework and the implementation of the relevant physics used to generate the results presented in this thesis. Then the results generated by *Trajectum* will be presented and compared to ALICE measurements. Finally the outlook of this research will be given.

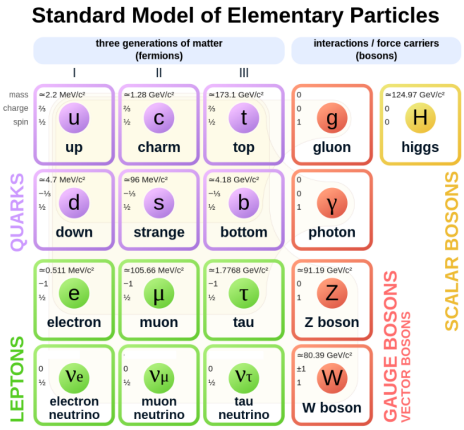

Figure 1: Visualization of the fundamental particles of nature in the Standard Model [25]

2 Theory

In this chapter all the relevant theory for the evolution of the QGP and heavy quarks within a heavy-ion collision will be covered. The goal of this section is to summarise the theories used to describe the hot and dense plasma. It will start by briefly summarizing the Standard Model and Quantum Chromodynamics (QCD). Then a description of relativistic hydrodynamics which describes the dynamics of the bulk QGP. This is followed by a description of the evolution of a heavy-ion collision in which the plasma is created and a section on the in medium evolution of heavy quarks. Finally a description of the different hadronization mechanisms of heavy quarks will be given.

2.1 Standard Model

The Standard Model of particle physics describes the fundamental building blocks and three of the four fundamental forces of nature, the electromagnetic, weak and strong nuclear force. These forces result from the exchange of the gauge bosons of each respective theory. The electromagnetic force is carried by the photon, the weak nuclear force is carried by the W and Z bosons and the gluon is responsible for the strong force. The Standard Model includes the electromagnetic, strong and weak forces and explains how these forces act on all of the matter particles shown in Fig. 1. In this thesis the main focus is on quarks and gluons which experience the strong force. In the Standard Model there are six different types of quarks with different masses and charge commonly referred to as quark flavours, up, down, strange, charm, beauty and top. The dynamics of quarks and gluons will be explained in the following section 2.2.

2.2 Quantum Chromodynamics (QCD)

Quantum Chromodynamics (QCD) is the theory governing the strong interaction. The strong interaction is described by a local, non-Abelian $SU(3)$ gauge theory. The fundamental charges connected to this gauge theory are called color charges and this theory describes the force that binds quarks into colorless hadrons. Within the standard model only quarks and gluons carry a color charge, so these are the only subatomic particles which 'feel' the strong force. Even though the color charge carried by quarks and gluons is unrelated to the everyday meaning of color, an analogy was drawn and the three individual colors in QCD were named red (r), green (g) and blue (b). These are the three distinct color charges which can take on different values. The QCD Lagrangian describes the dynamics of quarks and gluons. Since quarks are spin-$\frac{1}{2}$ particles the Lagrangian for a free quark is given by:

$$\mathcal{L}_q = \overline{\psi}(i\gamma^\mu \partial_\mu - m)\psi. \tag{2.1}$$

The quark field ψ is a three-component color-vector

$$\psi = \begin{pmatrix} \psi_r \\ \psi_g \\ \psi_b \end{pmatrix} \tag{2.2}$$

and each of the colour-vector components are four-component Dirac spinors. Since quarks and gluons both carry a color charge the QCD Lagrangian needs a contribution term for quarks, gluons and quark gluon interactions. The $SU(3)$ Lie group has 8 generators. A generator is an element within a group that can be used to produce all of the other elements of the group through repeated multiplication. In the context of quantum field theory, a generator can also be viewed as an operator corresponding to a symmetry transformation. For an $SU(3)$ gauge theory, such as QCD, the generators are the 8 Gell-Mann matrices $\frac{1}{2}\lambda_a$. Each generator of the group has one gluon field A^a_μ where μ denotes the spacetime coordinates and a goes from 1 to 8 representing each individual gluon field. To ensure local gauge invariance the partial derivative ∂_μ is replaced by a covariant derivative defined in terms of the generators and gauge fields of the group:

$$\partial_\mu \rightarrow D_\mu = \partial_\mu - igA_\mu, \tag{2.3}$$

where g is the coupling constant for strong interactions. The generators and gluon fields combined give a four-potential $A_\mu = 1/2\lambda_a A^a_\mu$ which leads to the interaction vertex between quarks and gluons. Replacing the four-gradient in equation 2.1 with the covariant derivative leads to the Lagrangian for quark-gluon interactions

$$\mathcal{L}_{q,qg} = \overline{\psi}(i\gamma^\mu D_\mu - m)\psi = \overline{\psi}(i\gamma^\mu \partial_\mu - m)\psi + \overline{\psi}(g\gamma^\mu A_\mu)\psi = \mathcal{L}_q + \mathcal{L}_{qg}. \tag{2.4}$$

The commutator of two covariant derivatives of the gauge theory describe the dynamics of the gauge boson, in this case the gluon. Therefore the field strength tensor is defined as:

$$F_{\mu\nu} = \frac{i}{g}[D_\mu, D_\nu] = \partial_\mu A_\nu - \partial_\nu A_\mu - ig[A_\mu, A_\nu]. \tag{2.5}$$

The $SU(3)$ gauge theory is non-Abelian because the generators, $\frac{1}{2}\lambda_a$, do not commute. Using the definition of the four-potential, $A_\mu = \frac{1}{2}\lambda_a A^a_\mu$, and the commutation relation $[\lambda_a, \lambda_b] = 2if^c{}_{ab}\lambda_c$, in which f^{abc} are the structure constants of the $SU(3)$ gauge theory, the gluonic field strength tensor can be written as:

$$F^a_{\mu\nu} = \partial_\mu A^a_\nu - \partial_\nu A^a_\mu + gf^a{}_{bc}A^b_\mu A^c_\beta. \tag{2.6}$$

The final term, $gf^a{}_{bc}A^b_\mu A^c_\beta$, which is due to the non-Abelian nature of $SU(3)$ gives rise to gluon self-interactions shown in the two diagrams on the right of Fig. 2. The contraction of two field-strength tensors is not gauge invariant, but the color trace is invariant.

$$Tr(F'_{\mu\nu}F'^{\mu\nu}) = Tr(UF_{\mu\nu}U^\dagger UF'^{\mu\nu}U^\dagger) = Tr(F_{\mu\nu}F^{\mu\nu}), \tag{2.7}$$

which is due to the cyclic property of the trace. Since the Lagrangian must be gauge invariant only the trace of the contraction of the gluon fields can appear in the gluon field Lagrangian, which is given by:

$$\mathcal{L}_g = -\frac{1}{2}Tr(F_{\mu\nu}F^{\mu\nu}). \tag{2.8}$$

So the final Lagrangian for QCD is:

$$\mathcal{L}_{QCD} = \mathcal{L}_q + \mathcal{L}_{qg} + \mathcal{L}_g = \overline{\psi}(i\gamma^\mu \partial_\mu - m)\psi + \overline{\psi}(g\gamma^\mu A_\mu)\psi - \frac{1}{2}Tr(F_{\mu\nu}F^{\mu\nu}). \tag{2.9}$$

This Lagrangian describes the interaction between quarks and gluons, shown in Fig. 2 and the propagation of a free quark.

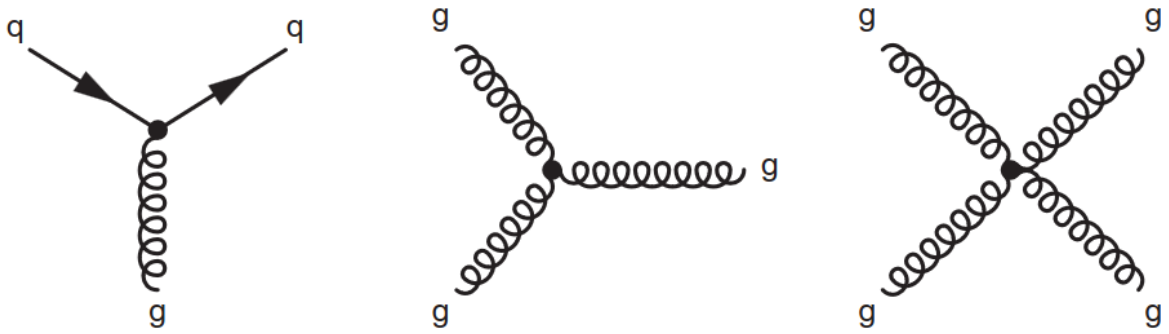

Figure 2: The three fundamental QCD interaction vertices [26]. The quarks are denoted by solid lines and the gluons are represented by the curly lines.

(a) Gluon-loop diagram

(b) Quark-loop diagram

Figure 3: Examples of fermionic and bosonic loop corrections to the gluon propagator leading to screening and anti-screening effects, respectively.

2.2.1 Running Coupling Constant and Perturbative QCD

When particles collide, they interact with one another. At high energies perturbative methods can be used to do calculations of these interaction processes. These perturbative methods are based on an expansion in powers of the strong coupling constant α_s, which measures the strength of the interactions between quarks and gluons. However, this coupling constant is not really a constant. The coupling constant depends on the four-momentum transferred across two vertices between interacting quarks and gluons, q^μ. This is due to loop corrections to the gluon propagator shown in Fig. 3, where a gluon can split into a quark anti-quark pair or two gluons.

Fig. 3b shows an example of a gluon splitting into a quark anti-quark pair. These fermionic loops lead to a screening effect which increases coupling strength at increasing momentum transfer just like an $e^+ + e^-$ loop correction to the photon propagator in Quantum Electrodynamics (QED). However, unlike photons in QED the gluons can interact with themselves creating a gluon loop shown in Fig. 3a. These gluon loops lead to an anti-screening effect which increases the coupling strength at decreasing momentum transfer. Introducing $Q^2 = -q^\mu q_\mu$ for momentum transfer and μ^2 as a reference scale at which the coupling strength is known, the evolution of $\alpha_s(Q^2)$ becomes:

$$\alpha_s(Q^2) = \frac{\alpha_s(\mu^2)}{1 + \beta_0 \alpha_s(\mu^2) ln(Q^2/\mu^2)}, \tag{2.10}$$

where $\beta_0 = \frac{11n-2f}{12\pi}$, n is the number of colours and f is the number of quark flavours. In the Standard Model there are six quark flavors and there are three colours. So β_0 is positive meaning that the anti-screening effect caused by the gluon loops is stronger than the screening effect caused by fermionic quark loops and α_s decreases with increasing Q^2 as illustrated in Fig. 4. More in depth information on the running coupling constant in QCD can be found in [27].

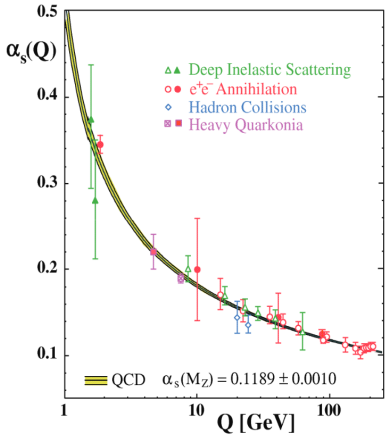

Figure 4: Running coupling constant in QCD [28]

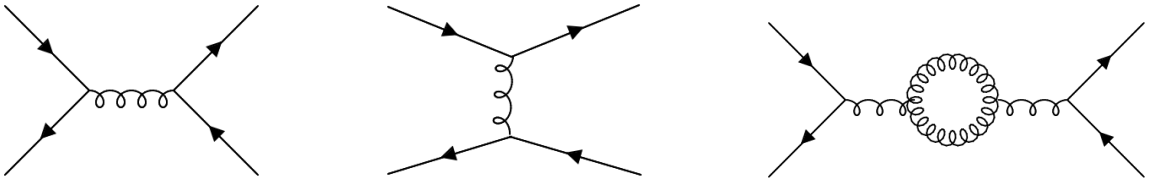

(a) $q\bar{q} \to q\bar{q}$ s-channel (LO) (b) $q\bar{q} \to q\bar{q}$ t-channel (LO) (c) $q\bar{q} \to q\bar{q}$ (NLO)

Figure 5: Examples of LO and NLO processes in which a quark and an anti-quark interact and produce another quark anti-quark pair

So, when the momentum transfer is large, the coupling is small. This means that quarks in hadrons behave almost like free particles when probed at large enough energies. This property of the strong interaction is known as asymptotic freedom. At small coupling, meaning high momentum transfer, perturbative QCD (pQCD) is valid. With perturbative QCD interaction processes between particles can be calculated up to a truncated order of the coupling constant. This is done by drawing Feynman diagrams consisting of the vertices shown in Fig. 2, and calculating the scattering cross-section by summing over all possible topologically distinct Feynman diagrams for a certain process. Typically this sum is only taken up to a certain order in the number of interaction vertices. Consider the process of a quark and an anti-quark interacting and producing another quark-antiquark pair shown in 5. The first two Feynman diagrams have two interaction vertices so they are of the order $\mathcal{O}(\alpha_s^2)$. The diagram on the right of 5 has three interaction vertices, so it is of the order $\mathcal{O}(\alpha_s^3)$. In a pQCD calculation of an interaction process the Feynman diagrams with the least number of interaction vertices representing that process will have the largest contribution and are called the leading order (LO) diagrams. Feynman diagrams representing the same process with the next smallest number of interaction vertices are called next to leading (NLO) and so forth. In perturbative calculations more interaction vertices means a smaller contribution to the calculation, since at high momentum transfer in which pQCD is valid, $\alpha_s \ll 1$.

Processes with high momentum transfer are referred to as hard processes. However, as the momentum exchange between colour charges decreases, the coupling strength becomes so strong that it is impossible to isolate a quark from a hadron. This phenomenon is called color confinement and it is the reason why we can not observe quarks directly. In the region of low momentum transfer the perturbative approach is no longer applicable and non-perturbative approaches such as lattice QCD (lQCD) [29–31]

and Effective Field Theories (EFT) [32,33] are used to calculate phenomena such as color confinement and the phase transition between the QGP and hadronic matter. The dynamics of the plasma are described by relativistic hydrodynamics which is discussed in the next section (2.3).

2.3 Relativistic Hydrodynamics

Relativistic hydrodynamics describes fluids at near lightspeed velocities in local thermal equilibrium. To acquire the relativistic fluid dynamic equations, the energy-momentum tensor $T^{\mu\nu}$ can be derived from the continuity equations.

$$\nabla_\mu T^{\mu\nu} = 0, \quad \nabla_\mu J^\mu = 0. \tag{2.11}$$

The energy-momentum tensor for an ideal relativistic fluid ($T^{\mu\nu}_{(0)}$) needs to contain the hydrodynamic degrees of freedom such as, energy density (ϵ), momentum density p, particle number density, a fluid velocity vector u^μ and it also must contain the metric tensor $g_{\mu\nu}$. The metric tensor used here is the Minkowski metric, $g_{\mu\nu} = \text{diag}(+,-,-,-)$ and the fluid velocity vector obeys the normalisation $g_{\mu\nu}u^\mu u^\nu = u^\mu u_\mu = 1$. $T^{\mu\nu}$ is symmetric and transforms as a tensor under Lorentz transformations, the most general form which symmetry allows is

$$T^{\mu\nu}_{(0)} = \epsilon(a_1 g^{\mu\nu} + a_2 u^\mu u^\nu) + p(a_3 g^{\mu\nu} + a_4 u^\mu u^\nu) \tag{2.12}$$

In the local restframe of the fluid, $u^\mu = \begin{pmatrix} 1 \\ \vec{0} \end{pmatrix}$. In this frame Pascal's law is valid, meaning the pressure exerted by a certain portion of the fluid is the same in all directions and perpendicular everywhere to the surface on which it acts [34]. So the space-like components $T^{ij}_{(0)}$ should be proportional to the pressure, $T^{ij}_{(0)} = p\delta^{ij}$. The $T^{00}_{(0)}$ component represents the proper internal energy density of the fluid, denoted by ϵ. These conditions lead to the following equations when imposed on 2.12

$$(a_1 + a_2)\epsilon + (a_3 + a_4)p = \epsilon, \qquad -a_1\epsilon - a_3 p = p \tag{2.13}$$

These equations imply that $a_1 = 0, a_2 = a_4 = 1, a_3 = -1$. So the energy-momentum tensor of an ideal relativistic fluid becomes

$$T^{\mu\nu}_{(0)} = \epsilon u^\mu u^\nu - p\Delta^{\mu\nu} \tag{2.14}$$

Where the tensor $\Delta^{\mu\nu} = g^{\mu\nu} - u^\mu u^\nu$ is introduced for later convenience. This tensor serves as a projection operator on the space orthogonal to the fluid velocity u^μ. It has the properties $\Delta^{\mu\nu}u_\mu = \Delta^{\mu\nu}u_\nu = 0$ and $\Delta^{\mu\nu}\Delta^\alpha_\nu = \Delta^{\mu\alpha}$. Without external sources the energy-momentum tensor is always conserved, $\partial_\mu T^{\mu\nu}_{(0)} = 0$. It proves useful to project these equations in the parallel and perpendicular directions to the fluid velocity, u_μ. For the parallel projection, one finds

$$\begin{aligned} u_\nu \partial_\mu T^{\mu\nu}_{(0)} &= u_\nu \partial_\mu [\epsilon u^\mu u^\nu - p\Delta^{\mu\nu}] = u^\mu \partial_\mu \epsilon + \epsilon(\partial_\mu u^\mu) + \epsilon u_\nu u^\mu \partial_\mu u^\nu - p u_\nu \partial_\mu \Delta^{\mu\nu} \\ &= (\epsilon + p)\partial_\mu u^\mu + u^\mu \partial_\mu \epsilon = 0 \end{aligned} \tag{2.15}$$

where the identity $u_\nu \partial_\mu u^\nu = \frac{1}{2}\partial_\mu(u_\nu u^\nu) = 0$ was used. For the perpendicular projection, one finds

$$\Delta^\alpha_\nu \partial_\mu T^{\mu\nu}_{(0)} = (\epsilon + p)u^\mu \partial_\mu u^\alpha - \Delta^{\mu\alpha}\partial_\mu p = 0. \tag{2.16}$$

$D = u^\mu \partial_\mu$, $\nabla^\alpha = \Delta^{\mu\alpha}\partial_\mu$ are introduced for the projection of derivatives parallel and perpendicular to the fluid velocity. ∇^α is the gradient in the fluid rest frame and D is the time derivative in the fluid rest frame, since in the fluid restframe $u^\mu = \begin{pmatrix} 1 \\ \vec{0} \end{pmatrix} \rightarrow D = u^0 \partial_0$. Rewriting equations (2.15) and (2.16) with the gradient and time derivative in the fluid restframe gives the following equations

$$\begin{aligned} &D\varepsilon + (\varepsilon + p)\partial_\mu u^\mu = 0 \\ &(\varepsilon + p)Du^\alpha - \nabla^\alpha p = 0 \end{aligned} \tag{2.17}$$

These are the fundamental equations for a relativistic ideal fluid [35].

By definition, in the ideal fluid picture all viscous effects are neglected. To include the effects of viscosity the energy momentum tensor becomes

$$T^{\mu\nu} = T^{\mu\nu}_{(0)} + \Pi^{\mu\nu} \tag{2.18}$$

With $\Pi^{\mu\nu}$ the viscous stress tensor that includes the contributions to the energy momentum tensor stemming from dissipation. Considering a system at zero chemical potential, all momentum density is due to the flow of energy density, $u_\mu T^{\mu\nu} = \varepsilon u^\nu \rightarrow u_\mu \Pi^{\mu\nu} = 0$ [35]. The fundamental equations of viscous fluid dynamics are found by projecting the conservation equations of the energy momentum tensor parallel and perpendicular to the fluid velocity. So with the inclusion of the viscous stress tensor and the choice of system the fundamental equations for relativistic viscous fluid dynamics are

$$\begin{aligned} &D\varepsilon + (\varepsilon + p)\partial_\mu u^\mu - \Pi^{\mu\nu}\nabla_{(\mu}u_{\nu)} = 0, \\ &(\varepsilon + p)Du^\alpha - \nabla^\alpha p + \Delta^\alpha_\nu \partial_\mu \Pi^{\mu\nu} = 0. \end{aligned} \tag{2.19}$$

An elegant way to derive expressions for $\Pi^{\mu\nu}$ is to use the second law of thermodynamics, which states that entropy always increases locally. Temperature, energy density, pressure and entropy density s, are all related through the same basic thermodynamic relations for a system with no chemical potential

$$\varepsilon + p = Ts, \; Tds = d\varepsilon. \tag{2.20}$$

In equilibrium the entropy 4-current $s^\mu = su^\mu$ and the second law of thermodynamics can be rewritten in the covariant form

$$\partial_\mu s^\mu = \partial_\mu (su^\mu) = u^\mu \partial_\mu s + s\partial_\mu u^\mu = Ds + s\partial_\mu u^\mu \geq 0. \tag{2.21}$$

So in combination with the thermodynamic relations (2.20) the second law (2.21) can be rewritten as

$$\partial_\mu s^\mu = Ds + s\partial_\mu u^\mu = \frac{1}{T}D\varepsilon + \frac{\varepsilon + p}{T}\partial_\mu u^\mu = \frac{1}{T}\Pi^{\mu\nu}\nabla_{(\mu}u_{\nu)} \geq 0. \tag{2.22}$$

Usually $\Pi^{\mu\nu}$ is split into a traceless part $\pi^{\mu\nu} \rightarrow \pi^\mu_\mu = 0$, and a leftover part with non-vanishing trace,

$$\Pi^{\mu\nu} = \pi^{\mu\nu} + \Delta^{\mu\nu}\Pi. \tag{2.23}$$

In a similar the a new notation for the traceless part of $\nabla_{(\mu}u_{\nu)}$ is introduced,

$$\nabla_{<\mu}u_{\nu>} \equiv 2\nabla_{(\mu}u_{\nu)} - \frac{2}{3}\Delta_{\mu\nu}\nabla_\alpha u^\alpha, \tag{2.24}$$

using the tracelesness of $\pi^{\mu\nu}$ and the operator definition $\Delta^{\mu\nu}\Delta^\alpha_\nu = \Delta^{\mu\alpha}$ the second law can be rewritten into:

$$\partial_\mu s^\mu = \frac{1}{2T}\pi^{\mu\nu}\nabla_{<\mu}u_{\nu>} + \frac{1}{T}\Pi\nabla_\alpha u^\alpha \geq 0. \tag{2.25}$$

Defining,

$$\pi^{\mu\nu} = \eta\nabla^{<\mu}u^{\nu>} = 2\eta\sigma^{\mu\nu}, \; \Pi = \zeta\nabla_\alpha u^\alpha, \tag{2.26}$$

for the bulk and sheer pressure, the inequality is guaranteed to be satisfied when $\eta \geq 0$ and $\zeta \geq 0$ [35]. With η and ζ the shear and bulk viscosity coefficients, respectively. In the non-relativistic limit $\Pi^{\mu\nu}$ becomes that of the Navier-Stokes equations [35]. However, this relativistic Navier-Stokes equation allows for superluminal propagation thereby violating causality. Proof for the violation of causality of

the relativistic Navier-Stokes equations is given in Apendix A of Ref [35]. This problem is solved by replacing the relations in (2.26) by the differential equations called the Israel-Stewart equations [36]:

$$D\Pi = -\frac{1}{\tau_\Pi(\varepsilon)}[\Pi + \zeta(\varepsilon)\nabla_\alpha u^\alpha] \tag{2.27}$$

$$\Delta^\mu_\alpha \Delta^\nu_\beta D\pi^{\alpha\beta} = -\frac{1}{\tau_\pi(\varepsilon)}[\pi^{\mu\nu} - 2\eta(\varepsilon)\sigma^{\mu\nu}] \tag{2.28}$$

The projectors in front of $D\pi^{\alpha\beta}$ ensure that the equation is traceless and orthogonal. τ_Π and τ_π are timescales over which the viscous pressures relax to the Navier-Stokes limit. The Israel-Stewart equations are the first-order hydrodynamic equations, since they contain derivatives up to the first order. So in summary, the Israel-Stewart equations (2.27) yield four different parameters, referred to as the first order transport coefficients:

$$\eta(\varepsilon), \quad \zeta(\varepsilon), \quad \tau_\pi(\varepsilon), \quad \tau_\Pi(\varepsilon) \tag{2.29}$$

The dependence on the energy density, or equivalently the temperature since temperature and energy density are directly related to one another, is made explicit. These transport coefficients envelop information about the underlying theory since they depend on the microscopic details of the theory. They also have an influence on macroscopic observables, which can be measured experimentally, since they enter the equations governing the hydrodynamical evolution. The Israel-Stewart equations (2.27) can be generalized even further by expanding the equations for bulk pressure and shear stress, which are derivative expansions up to first order derivatives, into second order hydrodynamics which contain derivatives up to the second order in the following form:

$$\begin{aligned} D\Pi = &-\frac{1}{\tau_\Pi(\varepsilon)}[\Pi + \zeta(\varepsilon)\nabla_\alpha u^\alpha + \delta_{\Pi\Pi}(\varepsilon)\nabla_\alpha u^\alpha \Pi \\ &- \lambda_{\Pi\pi}(\varepsilon)\pi^{\mu\nu}\sigma_{\mu\nu}] \end{aligned} \tag{2.30}$$

$$\begin{aligned} \Delta^\mu_\alpha \Delta^\nu_\beta D\pi^{\alpha\beta} = &-\frac{1}{\tau_\pi(\varepsilon)}[\pi^{\mu\nu} - 2\eta(\varepsilon)\sigma^{\mu\nu} + \delta_{\pi\pi}(\varepsilon)\pi^{\mu\nu}\nabla_\alpha u^\alpha \\ &- \phi_7(\varepsilon)\pi^{<\mu}_\alpha \pi^{\nu>\alpha} + \tau_{\pi\pi}(\varepsilon)\pi^{<\mu}_\alpha \sigma^{\nu>\alpha} - \lambda_{\pi\Pi}(\varepsilon)\Pi\sigma^{\mu\nu}] \text{ [23].} \end{aligned} \tag{2.31}$$

In both first and second order hydrodynamics the stress energy tensor is described by (2.18). The second order expansion adds the following transport coefficients:

$$\delta_{\Pi\Pi}(\varepsilon), \quad \lambda_{\Pi\pi}(\varepsilon), \quad \delta_{\pi\pi}(\varepsilon), \quad \phi_7(\varepsilon), \quad \tau_{\pi\pi}(\varepsilon), \quad \lambda_{\pi\pi}(\varepsilon).$$

Just like the first order transport coefficients, the second order transport coefficients can in prinicple be derived from the microscopic theory, and they could possibly be measured experimentally. These transport coefficients are very important for describing the quark-gluon plasma stage within the simulations of heavy ion collisions, since they characterize the dynamical properties of a fluid. Next, we will examine the evolution of a heavy-ion collision in which the QGP is created and how it freezes out to form hadrons.

2.4 Heavy Ion Collisions and the Quark-Gluon plasma

As mentioned in section 2.2 quarks and gluons are always confined into hadronic matter. However, at large temperatures and/or densities QCD matter udergoes a phase transition into a deconfined state. These temperatures can be reached by colliding heavy ions at ultra-relativistic energies in a small volume creating a very high energy density. When this system reaches thermal (near-)equilibrium a significant portion of the evolution of the heavy-ion collision will be described by a hot and dense QGP, which in turn can be described using hydrodynamics as discussed in section 2.3. The evolution

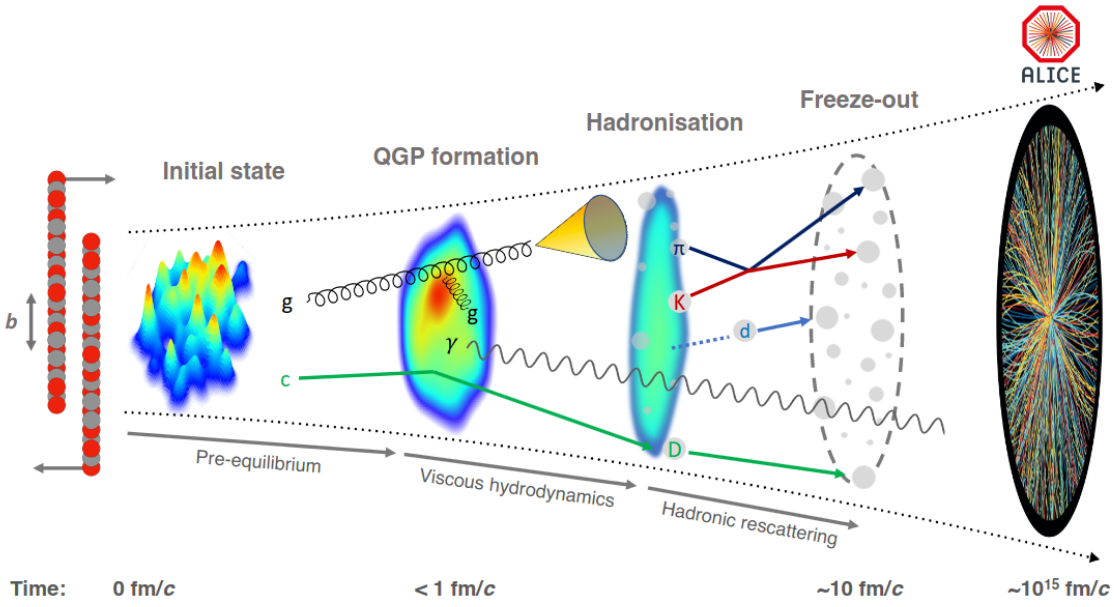

Figure 6: Visualisation of the evolution of a heavy-ion collision at LHC energies [37]

of a heavy-ion collision can be described by a series of different stages [37], which are visualised schematically in Fig. 6. These stages include: An initial state, determined by the wavefunction of the colliding nuclei; small and large-Q^2 interactions between partons drawn from colliding nucleons; equilibration and subsequent expansion of the QGP; chemical freeze-out of hadrons; a hadron resonance gas phase where hadrons interact and decay; stable particles fly freely to the detector. A more detailed review on the complete evolution of a heavy-ion collision is given in Ref. [2].

2.4.1 Initial Collision

Before the nuclei collide they will be highly Lorentz contracted into discs due to their ultra-relativistic velocities, as can be seen in Fig. 6. The distance between the center of each disc is the impact parameter, b. This impact parameter is closely related to the number of nucleons in each nucleus directly participating in the inelastic interaction, N_{part}. If we consider the nuclei as transparent we can count the number of inelastic nucleon-nucleon collisions between the left and right moving nuclei. The cumulative count of these inelastic nucleon-nucleon collisions is referred to as N_{coll}. For example, consider two nuclei with their constituent nucleons lined up in a row colliding head-on. If one nucleus has 3 nucleons and the other has 5, $N_{part} = 8$, but $N_{coll} = 15$. When the centers of each nucleus are close to each other, b is small. At small b, N_{part} and N_{coll} will be large, since large parts of the nuclei will overlap as they collide. When b is large N_{part} and N_{coll} will be small. Collisions with a small impact parameter are referred to as central i.e. head-on and collisions with large b are referred to as peripheral. In a real central heavy ion collision a nucleon which is located at the center of the nucleus will on average hit approximately 12 nucleons from the other nucleus, but it will hit fewer nucleons if it is located more on the edge of the collision [2]. This means that in central collisions N_{coll} is much larger than N_{part}. Due to the high number of binary nucleon-nucleon in central collisions more particles are produced than in peripheral collisions. Particle multiplicity, which is defined as the number of particles produced in a collision, therefore gives an experimental handle on collision centrality, since the centrality of a collision can not be directly measured [37]. As the heavy ions collide, most of the incident partons lose energy, but are not deflected by any large angle. Most of these interactions involve little transverse momentum (p_{T}) transfer, so they are considered soft. A small fraction of the

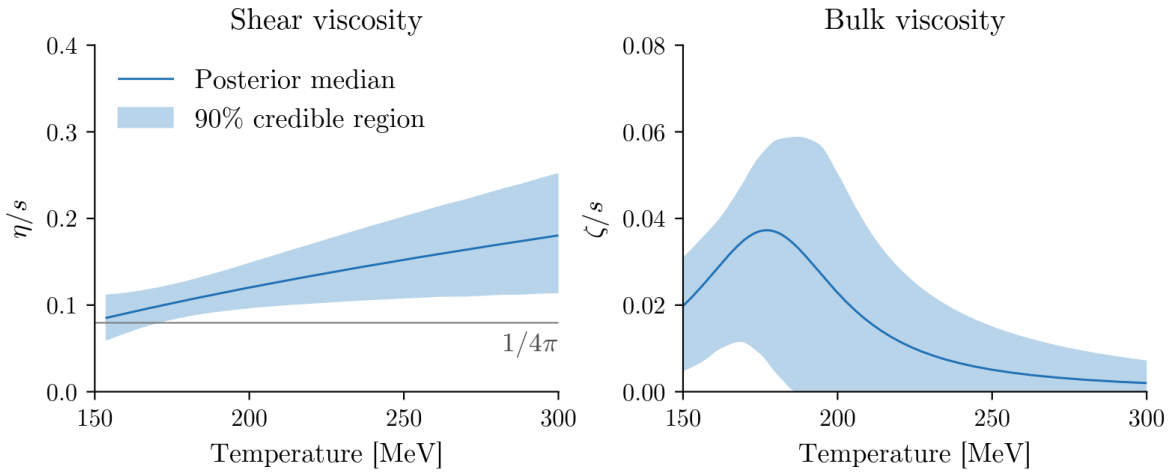

Figure 7: Estimated temperature dependence of the specific shear and bulk viscosity divided by entropy density. Figure taken from [41].

incident partons undergo hard perturbative interactions with high transverse momentum transfer, this leads to the production of particles with high p_{T} [2]. The partons within the nuclei that are involved in the soft interactions determine the overal entropy deposition and energy density of the initial state. The hard perturbative processeses from large Q^2 interactions are mostly driven by N_{coll}. These hard interactions enable the production of high momentum/mass quarks. These heavy quarks (HQs) are considered heavy for two distinct reasons. The first reason is that the mass of the quark is larger than the QCD scale parameter Λ_{QCD}. The QCD scale parameter characterizes the transition between the weak and strong coupling regimes. It essentially signifies the energy scale below which quarks and gluons become confined. So since, $m_Q \gg \Lambda_{QCD}$ the evaluation of the cross-section and p_{T} spectra with perturbative QCD schemes becomes possible [8]. The second reason is that $m_Q \gg T$ meaning that the HQ mass is much larger than the temperature of the plasma, which implies that thermal production of heavy quarks in the QGP is expected to be negligible contrary to the thermal production of light quark flavors. Therefore the heavy quark production is set by the initial hard scatterings. These two scale hierarchies in combination with the fact that heavy quarks are produced initially, with a $\tau_0 < O(10^{-}1)$ fm/c [38], make them excellent probes since they witness the entire evolution of the plasma.

2.4.2 QGP Formation

After the initial collision, when the nuclei are moving away from each other, they leave matter behind them. Up to a good approximation this matter is produced in a way that is boost-invariant in the beam direction, meaning the axis along which the nuclei travel. Some time after the initial collision this matter will hydrodynamise and the system can be described by hydrodynamics. This is different from thermalization since the matter is not yet in equilibrium at this stage and large gradients of the stress-energy tensor exist. The process of hydrodynamization is poorly understood and the formation time is also subject to discussion. Kinetic theory states that it will occus after approximately 1 fm/c [39], whilst holographic calculations predict an earlier formation of this stage after roughly 0.35 fm/c [40]. On top of that, different models for the hydrodynamization process provide different answers for the initial state of the hydrodynamic fluid right after hydrodynamization.

2.4.3 Hydrodynamical evolution of the QGP

When the hydrodynamic fluid is formed the next stage of the description of the evolution of the heavy-ion collision is viscous relativistic hydrodynamics. Viscous hydrodynamics is well understood, but what is less understood are the values of the transport coefficients coming into the evolution through equations (2.30-2.31). The transport coefficients with the most visible effect on the experimental observables are the bulk and shear viscosities. This is logical, since hydrodynamics is a derivative expansion, and higher order derivatives are assumed to contribute less to the evolution of the system. The only first order coefficients entering the evolution are the bulk and shear viscosities, so they have the most influence on the evolution of the plasma and therefore on the measured experimental observables. A fluids "quality" is determined by its specific shear viscosity, which is the dimensionless ratio between the shear viscosity and the entropy density s, η/s. The entropy density is a proxy for the number density, so the specific shear viscosity is in essence a viscosity per unit. A remarkable feature of the QGP is that the specific shear viscosity is very small $\eta/s \approx 1/4\pi$. Which means the plasma is nearly a perfect fluid. The temperature dependence of the specific shear viscosity is shown on the left in Fig. 7. But what is the effect of the specific shear viscosity on hydrodynamics, and what is the link to experimental observations of heavy-ion collisions? Most apparent is the impact that the specific shear viscosity has on the flow and collective behaviour of the system. Anisotropic flow of the hot and dense medium can be measured experimentally, it is a measure of the amount of hydrodynamic collective motion developed in the QGP [16]. The anisotropic flow parameters v_n are defined as the Fourier coefficents of final state particle azimuthal angle distributions with respect to the collision event plane.

$$\frac{dN}{d\varphi} \propto 1 + 2\sum_{n=1}^{\infty} v_n cos[n(\varphi - \Psi_n)] \tag{2.32}$$

Where Ψ_n is the event-plane angle. The second order harmonic flow coefficient v_2 is called elliptic flow and is often the largest coefficient in heavy-ion collisions. A higher shear viscosity would create a more isotropic system and therefore reduce the anisotropic flow [41]. So the anisotropic flow parameters v_n are the primary viscometer for the QGP.
Bulk viscosity ζ is related to the rate of expansion of the fluid, which can be seen from the way it enters equation (2.30). It impacts the evolution of the QGP predominantly by diminishing the radial expansion rate, thereby leading to a decrease in the transverse momentum observed in emitted particles.

2.5 Heavy Quark Diffusion

As mentioned in subsection 2.4.1 heavy quarks are very good probes of the QGP since they witness the entire evolution of the system. Another benefit of the high mass of heavy quarks is that due to their high masses, they are expected to be influenced less by the hot and dense medium than light parton flavors [42]. To study the in medium parton evolution and energy loss, two mechanisms are often considered: quasi elastic scattering of the quarks with the in medium partons and gluon radiation induced by the medium. These two energy loss mechanisms are called collisional and radiative enrgy loss, respectively. Collisional energy loss is considered to be the dominant energy loss mechanism for heavy quarks, especially at low energies [42, 43]. This is due to a phenomenon called the "dead-cone effect" [44], where the large masses of the heavy quarks suppress the phase space of gluon radiation. For small momentum transfers, the multiple scatterings of heavy quarks with thermal partons within the QGP medium can be treated as Brownian motion and is commonly described using the Langevin equation [45]. In this work, the only energy loss considered is collisional energy loss. So the motion of the heavy quarks inside the thermalized medium can be described by the Langevin equation, expressed

in terms of their position and momentum:

$$dx_i = \frac{p_i}{E_i} dt,$$
$$dp_i = \left(F_i^{\text{Drag}} + F_i^{\text{Diff}}\right) dt, \tag{2.33}$$

where dx_i and dp_i are the changes in position and momentum in the ith time step dt of the heavy quark [45]. The drag force component of this equation is given by:

$$F_i^{\text{Drag}} = -\eta_D(p_i) p_i, \tag{2.34}$$

where $\eta_D(p_i)$ is the drag coefficient. The other term in equation (2.33), $F_i^{\text{Diff}} = \xi_i$ is just a thermal noise term. This thermal noise can be dependent on the heavy quark momentum, but in this work, for the sake of simplicity, we do not consider such dependence. The random momentum kicks generated by the thermal noise satisfy the following correlation relation [46]:

$$\langle \xi^i(t) \xi^j(t') \rangle = \kappa \delta^{ij} \delta(t - t'). \tag{2.35}$$

Where κ is the momentum diffusion coefficient, this momentum diffusion coefficient can be linked to the drag coefficient through the dissipation-fluctuation relation in the non-relativistic approximation:

$$\eta_D(p) = \frac{\kappa}{2TE}. \tag{2.36}$$

In the limit of low momentum transfer this becomes:

$$\eta_D = \frac{\kappa}{2Tm_Q}. \tag{2.37}$$

This can be connected further to the spatial diffusion coefficient which is directly related to the thermal relaxation/equilibration time τ_Q of the heavy quark via [47]

$$\tau_Q = \frac{m_Q}{T} D_s, D_s = \frac{T}{m_Q \eta_D(0)} = \frac{2T^2}{\kappa}. \tag{2.38}$$

The spatial diffusion coefficient D_s is often scaled by the thermal wavelength $\lambda_{th} = 1/(2\pi T)$ of the QGP medium to create a dimensionless quantity $D_s/\lambda_{th} = (2\pi T D_s)$ which quantifies all relevant components: the drag force (2.34) and the thermal random force (2.35) within the Langevin approach. So the interactions between the QGP medium and the heavy quarks are all conveniently encoded within $2\pi T D_s$. This spatial diffusion constant is a proxy for the coupling strength of the heavy quark with the thermal medium. A small value for D_s means that frequent rescattering of the heavy quark limits its spatial dispersion, so it characterizes a strong coupling to the medium. In Fig. 8 the temperature dependence of the charm quark spatial diffusion constant is shown. The datapoints in this figure represent the spatial diffusion coefficient as calculated through quenched lattice QCD [48, 49]. Whilst the colored bands are visualizations of potential-based T-matrix calculations [50, 51]. The dash-dotted line is the spatial diffusion coefficient as calculated through perturbative QCD [52]. The x-axis is scaled by T_c which is the critical temperature below which a deconfined QGP can no longer be sustained and the system will undergo a phase transition into hadronic matter.

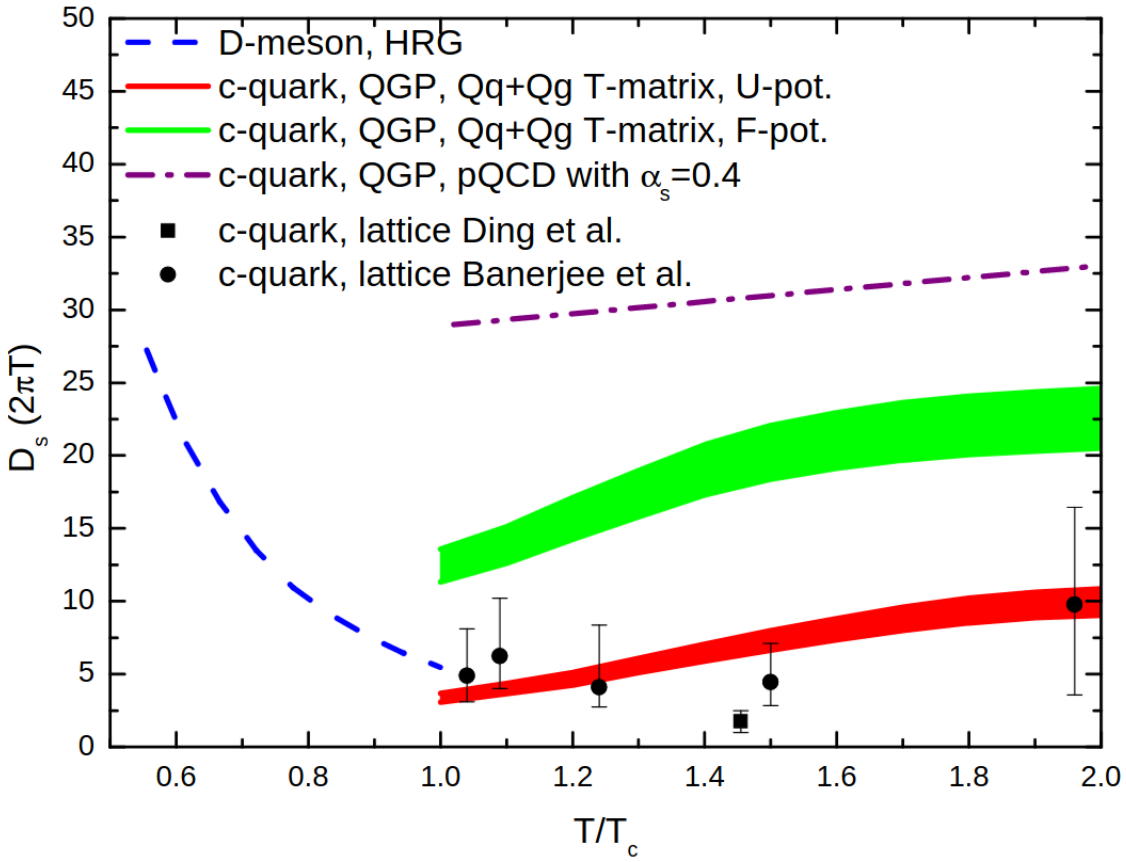

Figure 8: Charm quark spatial diffusion coefficient scaled with the thermal wavelength, in the QGP ($T > T_c$) and for D mesons in hadronic matter ($T < T_c$). The bands are potential-based T-matrix calculations, and the data points are extracted from quenched lattice QCD. [53]

2.6 Heavy Quark Hadronization

After cooling down the QGP can no longer maintain local hydrodynamic equilibrium and it can no longer be described by hydrodynamics. At this stage the constituents of the plasma will "freeze out" chemically and form particles. It is important to note that this does not happen instanteneously throughout the QGP. This occurs when the local temperature within the plasma drops below the critical temperature T_c, meaning that this process is continuous since there are temperature gradients within the QGP. This process is called hadronization. Shortly after all particles have frozen out they will still interact and decay. These decaying particles will decay further, forming a hadronic cascade. As the system expands particles will no longer interact, with the exception of unstable particle decays, and the particles will travel in straight trajectories. The lifetime of these particles is long enough for them to reach the detector and they are the only things that can be observed directly from a heavy-ion collision and they carry information about the different stages of the evolution of the heavy-ion collision. As mentioned earlier in section (2.4.1), heavy quarks are suited for probing the dynamical properties of the QGP. So in this thesis the focus partially lies on heavy quark hadronization, which is different from the hadronization of light quarks. There are two ways in which a heavy quark can hadronize into a hadron, fragmentation and coalescence. When a heavy quark fragments it picks up a light quark/quarks from quark-antiquark pairs created by a radiated gluon and together the heavy and light quark form into a hadron. Fragmentation is the dominant hadronization mechanism at high transverse momentum. However, at low momenta a heavy quark is more likely to hadronize through

a coalescence/recombination mechanism. In the case of coalescence, the heavy quark combines with thermal quarks from the QGP medium. The probability of a heavy quark to combine with thermal quarks into a hadron depends on the overlap of the wave functions of the constituent partons with the wave function of the combined hadron. The next sections will give more in depth information on the mathematical approach for fragmentation and coalescence models.

2.6.1 Fragmentation

The fragmentation process describes the transition of perturbative objects (quarks and gluons) into confined hadrons. Processes involving fragmentation are described by separating the contributions to the process into a perturbative and non-perturbative part [54]. The calculation is usually done by convoluting the perturbative heavy quark production cross-section with a non-perturbative fragmentation function which describes the decrease in the momentum of the heavy quark as it hadronizes:

$$\frac{d\sigma_H}{dp_{\mathrm{T}}}(p_{\mathrm{T}}) = \int \frac{dz}{z} D^{np}_{Q\to H}(z) \frac{d\sigma^{pert}}{dp_{\mathrm{T}}}\Big(\frac{p_{\mathrm{T}}}{z}\Big). \tag{2.39}$$

In this formula $D^{np}_{Q\to H}(z)$ is the non-perturbative fragmentation function and z is the fraction of momentum carried over from the primordial heavy quark to the fragmented hadron. Note that this formula is not the result of rigorous theoretical calculation, but more so the result of logical assumptions. Moreover it is subject to very large uncertainties in the region where the heavy quark p_{T} is not much larger than its mass m.
The main characteristics of the non-perturbative fragmentation function $D^{np}_{Q\to H}(z)$ can be identified by basic QCD arguments. It was recognized early [55] that the fragmented hadron should retain a large amount of the momentum of the primordial heavy quark. Furthermore it was argued that the average momentum lost by the quark when fragmenting was given by:

$$\langle z \rangle \approx 1 - \frac{\Lambda_{QCD}}{m}. \tag{2.40}$$

From this equation it becomes obvious that the non-pertubarbative fragmentation function of the heavy quark must be very hard, i.e. it loses little momentum when hadronizing, since $\Lambda_{QCD} \ll m_Q$. In the limit of a very heavy quark the fragmentation function is expected to be peaked near $z = 1$. This can also be seen from a very basic argument: a fast-travelling massive quark will only lose very little speed, and therefore momentum, when it picks up a light quark from the vacuum by radiating an energetic massless gluon [54]. Thus the shape of the non-perturbative fragmentation function will show a peak that becomes increasingly centered around $z = 1$. Some of the most used fragmention functions are:

- Peterson *et al.* [56]:
$$D^{np}_{Q\to H}(z) \propto \frac{1}{z}\Big(1 - 1/z - \frac{\epsilon}{1-z}\Big)^{-2}, \tag{2.41}$$
- Kartvelishvili *et al.* [57]:
$$D^{np}_{Q\to H}(z) \propto z^{\alpha}(1-z), \tag{2.42}$$
- Collins & Spiller [58]:
$$D^{np}_{Q\to H}(z) \propto \Big(\frac{1-z}{z} + \frac{(2-z)\epsilon_C}{1-z}\Big)(1+z)^2\Big(1 - 1/z - \frac{\epsilon_C}{1-z}\Big)^{-2}, \tag{2.43}$$
- Bowler [59]:
$$D^{np}_{Q\to H}(z) \propto z^{-(1+bm^2_{h,\perp})}(1-z)^a \exp\Big(-\frac{bm^2_{h,\perp}}{z}\Big), \tag{2.44}$$

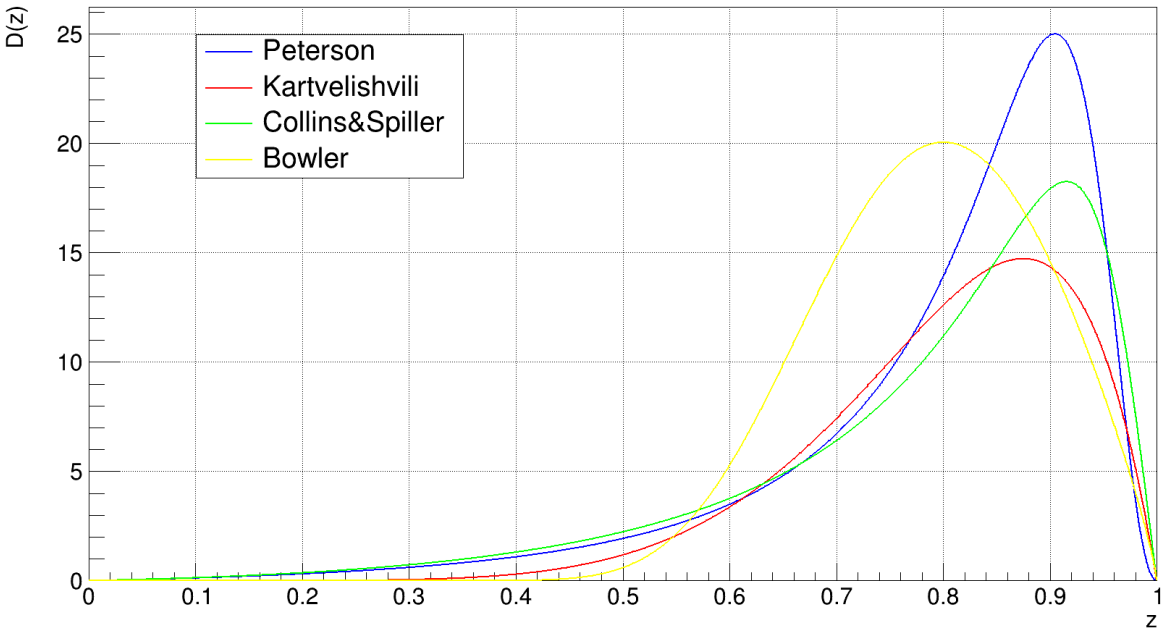

Figure 9: Visualization of different fragmentation functions.

where $\epsilon, \alpha, \epsilon_C, a, b$ and $m_{h,\perp}$ are all non-perturbative parameters dependent on the fragmented hadron species. These parameters are fixed by fitting the calculated p_{T}-differential cross-section of a certain hadron species obtained in equation (2.39) to the p_{T}-differential cross-section measured in data. Fig.ure 9 shows the different fragmentation functions listed in this section. Notice that all these functions are peaked near $z = 1$. Which means that the heavy hadron will retain a large part of the momentum of the primordial hadronized heavy quark as is required.

2.6.2 Coalescence

Hadronization purely through fragmentation can not reproduce various measured observables, such as anisotropic flow and baryon to meson ratios in Pb-Pb collision [18], [60], [13]. However, these observables have been calculated correctly using a hybrid hadronization approach through both fragmentation and coalescence [21]. The basic idea behind heavy quark coalescence is that a heavy quark within the QGP can combine with a comoving thermal parton within the medium adding up their respective momenta. Especially at low to intermediate momenta coalescence is believed to be the main hadronization mechanism [61].
In this work we base our coalescence mechanism on the "sudden recombination" model for coalescence developed by [62]. The momentum distributions for produced mesons and baryons in a sudden recombination model are determined by the following expressions [45]:

$$\begin{aligned}
\frac{dN_M}{d^3p_M} &= \int d^3p_q d^3p_Q \frac{dN_q}{d^3p_q}\frac{dN_Q}{d^3p_Q} f_M^W(\vec{p}_q, \vec{p}_Q)\delta(\vec{p}_M - \vec{p}_q - \vec{p}_Q), \\
\frac{dN_B}{d^3p_B} &= \int d^3p_{q1} d^3p_{q2} d^3p_Q \frac{dN_{q1}}{d^3p_{q1}}\frac{dN_{q2}}{d^3p_{q2}}\frac{dN_Q}{d^3p_Q} f_B^W(\vec{p}_{q1}, \vec{p}_{q2}, \vec{p}_Q)\delta(\vec{p}_B - \vec{p}_{q1} - \vec{p}_{q2} - \vec{p}_Q).
\end{aligned} \tag{2.45}$$

In these equations $f_M^W(\vec{p}), f_B^W(\vec{p})$ are the Wigner functions of the constructed meson or baryon and $\frac{dN_q}{d^3p_q}, \frac{dN_Q}{d^3p_Q}$ are the momentum distributions of a valence light and heavy quark in the recombined heavy flavour meson or baryon. Within *Trajectum* we only consider heavy flavour baryons with one heavy

quark as can be seen from equation (2.45). For light quarks and antiquarks within the QGP we use the Fermi-Dirac distribution as the momentum distribution in their local fluid cell:

$$\frac{dN_q}{d^3p} = \int d^3p \frac{g_q V}{e^{E/T_c}+1}, \tag{2.46}$$

where $g_q = 6$ represents the spin and color degeneracies of the light quark and a uniform distribution throughout position space is assumed inside volume V. This momentum distribution is then integrated numerically to yield the light quark density at the freeze-out temperature. The wave function of a meson can be approximated by the ground-state wave function of a simple quantum harmonic oscillator, from this the Wigner function in momentum-space for a meson can be calculated and it is given by [45]:

$$f_M^W(q^2) = N g_M \rho_q \sigma^3 e^{-q^2\sigma^2}. \tag{2.47}$$

Where N is a normalization constant which makes sure that when a heavy quarks momentum $p_Q = 0$ the probability for that heavy quark to coalesce is 1, g_M is a statistic factor which takes the color and spin degrees of freedom into account and ρ_q is the light quark density at the freeze-out temperature. $q^2 = \vec{q}\cdot\vec{q}$ and $\vec{q}$ is the relative momentum between the two particles defined in the center-of-mass frame of the meson:

$$\vec{q} \equiv \frac{1}{E_q' + E_Q'}(E_Q\vec{p}_q' - E_q\vec{p}_Q'). \tag{2.48}$$

The width parameter σ in equation (2.47) is related to the harmonic oscillator frequency ω through the relation $\sigma \equiv 1/\sqrt{\mu\omega}$, $\mu = m_q m_Q/(m_q + m_Q)$ is the reduced mass of the heavy flavour meson.
The Wigner function for a heavy flavour meson can be further extended to a three-particle system for baryon production. This is done by averaging over all ways to first recombine two quarks and then adding the third one. This leads to the following equation:

$$f_B^W(q_1^2, q_2^2) = N g_B \rho_q^2 \sigma^6 e^{-\sigma^2(q_1^2+q_2^2)}, \tag{2.49}$$

q_1 and q_2 are defined in the center-of-mass frame of the produced baryon:

$$\vec{q}_1 \equiv \frac{1}{E_1' + E_2'}(E_2'\vec{p}_1' - E_1'\vec{p}_2'), \qquad \vec{q}_2 \equiv \frac{1}{E_1' + E_2' + E_3'}[(E_1' + E_2')\vec{p}_3' - E_3'(\vec{p}_1' + \vec{p}_2')], \tag{2.50}$$

and for the baryon the reduced mass is:

$$\mu = \frac{m_q m_Q}{2m_Q + m_q}. \tag{2.51}$$

The reduced mass is the same for all charm baryons since we use a thermal mass of 300 MeV for the light u,d,s constituents of the QGP, so $m_q = m_s = m_d = m_u$. This is a reasonable assumption for the up and down quarks, but the thermal strange quark mass is often considered to be higher.
The Wigner functions in equations (2.47, 2.49) are directly related to the probability of forming a hadron through coalescence. So due to their Gaussian nature it becomes obvious that the probability of forming a hadron through coalescence is high if the relative momentum difference between the quark constituents of the hadron is small

Trajectum employs a hybrid hadronization model, meaning that heavy quarks can either fragment or recombine. The hadronization method of the heavy quark depends on its momentum and on the light quark density in the QGP as the temperature reaches the freeze-out temperature. *Trajectum* simulates a heavy-ion collision up until the chemical freeze-out. So after the entire QGP has cooled down below the freeze-out temperature $T < T_c$ and all particles have hadronized the simulation ends. The next section will briefly summarize the *Trajectum* framework.

3 Trajectum

Trajectum is a state of the art heavy ion simulation code created by, [23]. The code consists of three different executables. Collide, Analyze and Collect. Collide simulates the collision from its pre-equilibrium stage, to its hydrodynamical stage and subsequently calculates the freeze-out surface after which the code goes from a continuous hydrodynamical description towards a discrete particle description. After all particles have frozen out the collide executable is finished. The output of the collide executable can be fed into a hadronic afterburner, i.e., UrQMD [63] or SMASH [64]. Which simulates the interactions of the particles produced by the collide executable up to the point where the particles can be considered as non-interacting and also simulates the decay of unstable particles. The output of the afterburner or the collide output directly after the freeze out can then be used by the analyze executable to calculate the observables of the collision with the weight of each event taken into account. The collect executable then collects all data and outputs a mathematica file for further data processing. In the following subsections a more in depth explanation of each executable will be given.

3.1 Collide

As previously mentioned collide simulates three distinct stages of a collision. The pre-equilibrium, hydrodynamical and hadronic stage. The pre-equilibrium stage generates the initial conditions for the hydrodynamical evolution of the QGP. These initial conditions are passed to the component of the code which handles the hydrodynamical evolution, the hydrodynamics model. The hydrodynamics model then evolves the system through time step by step. For this evolution the model depends on two auxiliary components:

- Transport coefficients, which contains the equation of state together with the first and second order transport coefficients as discussed in section 2.3.
- Partial differential equation (PDE) solvers, which implement an algorithm for the solving of partial differential equations.

After the computation of each time step by the hydrodynamics model, the new state of the fluid is handed to the final component of collide, the hadronizer. The hadronizer computes the freeze-out surface and generates particles from the QGP. After the last computed time step the hadronizer ends the computation when there is no new addition to the freeze-out surface and collide will move on to the next event. In summary there are five components which make up the collide executable and together simulate the collision:

- Initial conditions
- Hydrodynamics model
- Transport coefficients
- PDE solver
- Hadronizers

The next subsections will explain these components in short. Ref [23] gives an in depth explanation for each component.
An important point to note is that throughout this work boost invariance is assumed. This means that we solve hydrodynamics in 2+1D, we do this by taking the Milne metric:

$$ds^s = d\tau^2 - dx^2 - dy^2 - \frac{d\eta^2}{\tau^2}, \tag{3.1}$$

this metric is related to the Minkowski metric through the coordinate transformation:

$$\tau = \sqrt{t^2 - z^2}, \qquad \eta = \frac{1}{2} log\Big(\frac{t+z}{t-z}\Big). \tag{3.2}$$

Where τ is the proper time and η is the pseudorapidity. This metric makes boosts correspond to shifts in pseudorapidity and boost invariance can be implemented by assuming that there is no η-dependence in any of the variables constituting the fluid.

3.2 Initial conditions

The initial conditions component within collide provides the initial conditions for the hydrodynamical evolution. Within *Trajectum* there is a choice between four different sets of initial conditions:

- Monte Carlo Glauber [65–68]
- Ohio State University [69, 70]
- TRENTo [71],
- Gubser flow [72–74]

The initial conditions used throughout this work are the TRENTo [71] initial conditions. This is a phenomenological model which describes the initial state of a heavy ion collision. TRENTo also includes a model for the evolution from the proper time of collision $\tau = 0^+$ up to the moment when hydrodynamical evolution is started, this is called the free-streaming time τ_{fs}.
The first step to calculating the initial conditions for the hydrodynamical model is to determine the positions of nucleons within the colliding nuclei. For two colliding protons this is trivial, since a proton is by definition a nucleon. To determine the nucleon positions for other nuclei, we assume that the distribution of nucleons within the nucleus follows a Saxon-Woods distribution [75, 76]:

$$\rho(r, \theta, \phi) = \rho_0 \frac{1 + w(r/R(\theta))^2}{1 + \exp\Big(\frac{r - R(\theta)}{a}\Big)}, \tag{3.3}$$

ρ is the probability density to find a nucleon at spherical coordinates (r,θ, ϕ). In this equation ρ_0 is a normalization constant, R is the radius of the nucleus, a represents the depth of the 'skin' of the nucleus and w corresponds to deviations from a spherical shape. [75]. Since the only heavy ions collided in this work are lead (Pb^{208}) ions and we assume no spherical deformation and a constant nuclear radius ($R(\theta) = R$), the parameters for this distribution are set according to Ref. [77] and are given in Table 1. TRENTo initial conditions also mimic a hard-core repulsion potential between nucleons by requiring that the distance between two nucleons is greater than a pretedermined minimal distance d_{min}. In this work this minimal distance is set at $d_{min} = 0.8001$ fm. So nucleon positions are sampled from the Saxon-Woods distribution (3.3), with the parameters set to the ones given in Table 1 whilst enforcing the minimal distance requirement.
After all nucleon positions in both ions are known, the number of participating nucleons, or 'wounded' nucleons, are calculated. From these participating nucleons TRENTo initializes the plasmas stress-energy tensor at time τ_{fs}. When all initial conditions for the plasma have been determined the hydrodynamics model calculates the evolution of the plasma.

3.3 Hydrodynamics Model and Transport Coefficients

Within collide both first and second order hydrodynamics as discussed in section 2.3 can be used to calculate the evolution of the plasma. The transport coefficients model is tasked with computing the pressure of the plasma through an equation of state (EoS). In this work the EoS used is a Lattice

Nucleus	R (fm)	a (fm)	w (fm)
^{208}Pb	6.68	0.447	0

Table 1: Parametrization of the Saxon-Woods distribution for a ^{208}Pb ion used in collide. Parameters taken from Ref. [77]

QCD equation of state with a temperature dependence in some of the transport coefficients and we use second order hydrodynamics. For the equation of state the following parametrization is used [78]:

$$\frac{P}{T^4} = \frac{1}{2}(1 + tanh[c_t(t - t_0)])\Big(\frac{p_i d + a_n/t + b_n/t^2 + d_n/t^4}{1 + a_d/t + b_d/t^2 + d_d/t^4}\Big). \tag{3.4}$$

All parameters in this equation are the same as the ones used in Ref. [23].
Since a temperature dependent EoS is used in this work, the shear and bulk viscosities are also dependent on temperature [41]:

$$\frac{\eta}{s}(T) = \begin{cases} (\eta/s)_{\text{hrg}} & T < T_c, \\ (\eta/s)_{\text{min}} + (\eta/s)_{\text{slope}}\dot{(}T - T_c)\dot{(}\frac{T}{T_c}^{(\eta/s)_{\text{crv}}}) & T > T_c, \end{cases}$$
$$\frac{\zeta}{s}(T) = \frac{(\zeta/s)_{\text{max}}}{1 + \left(\frac{T - (\zeta/s)_{T_0}}{(\zeta/s)_{\text{width}}}\right)^2},$$

where T_c is the freeze-out temperature, and

$$(\eta/s)_{\text{hrg}}, \quad (\eta/s)_{\text{min}}, \quad (\eta/s)_{\text{slope}}, \quad (\eta/s)_{\text{crv}}, \quad (\zeta/s)_{\text{max}}, \quad (\zeta/s)_{T_0}, \quad (\zeta/s)_{\text{width}}$$

are parameters which have been fixed by a Bayesian analysis in Ref. [41]. The shear and bulk relaxation times have been calculated in Ref. [79], and are defined by the following constants:

$$\frac{\tau_\pi sT}{\eta}, \qquad \frac{\tau_\Pi sT(1/3 - c_s^2)^2}{\zeta},$$

where c_s is the speed of sound. The second order hydrodynamic coefficients used are given by the following constants [79]:

$$\frac{\delta_{\pi\pi}}{\tau_\pi}, \quad \frac{\phi_7}{P}, \quad \frac{\tau_{\pi\pi}}{\tau_\pi}, \quad \frac{\lambda_{\pi\Pi}}{\tau_\pi}, \quad \frac{\delta_{\Pi\Pi}}{\tau_\Pi}, \quad \frac{\lambda_{\Pi\pi}}{\tau_\Pi(\frac{1}{3} - c_s^2)},$$

which have been fixed in a previous Bayesian parameter analysis [24]. *Trajectum* solves the hydrodynamics equations with a partial differential equation (PDE) solver. The PDE solver used in this work is the MUSCL solver, which is guaranteed to be stable. This solver interfaces with the hydrodynamics model which gives the hydrodynamical functions to solve and the solver updates the state of the plamsa from proper time τ to $\tau + \Delta\tau$. After each timestep $\Delta\tau$ the updated plasma state is handed over to the hadronizer which generates particles from the plasma.

3.4 Hadronizer

Heavy quarks are hadronized through fragmentation and coalescence as discussed in sections 2.6.1 and 2.6.2. The hadronization method used in *Trajectum* for light quarks is the Cooper-Frye hadronization method [80]. The first step in this particlization proces is computing the freeze-out surface. This is an isotherm of a user specified temperature T_{fr}. After calculating the freeze-out surface the next step is

to generate particles from the fluid. A number of particles is generated according to Poisson statistics and the particles are generated using the Cooper-Frye formula [80]:

$$E\frac{dN_i}{d^3p} = \frac{g_i}{(2\pi)^3}\int_\sigma \frac{1}{exp(p\cdot u/T)\pm 1}p^\mu d^3\sigma_\mu. \tag{3.5}$$

With g_i the number of degrees of freedom for particle species i and σ_μ the local surface normal. This formula is designed in a way that the hadronization process is not a change in physical processes, but rather a change in the description of the process, such that the particles are produced in a way that the stress-energy tensor remains continuous on average across the freeze-out surface.
After all particles have frozen out *Trajectum* terminates the simulation and it outputs 5 files. An input file which contains all the parameters the user gave to collide, a geometry file describing the collision geometry, an extra file containing the generated initial conditions and two particle files which contain particle positions, momenta and identities. One particle file contains the lighter hadrons which can be decayed with a hadronic afterburner like UrQMD or SMASH. The other particle file contains heavy particles which need to bypass the hadron cascade.

3.5 Analyze

After collide has calculated the particle positions, momenta and identities after the freeze-out, the analyze executable is tasked with calculating observables from the particle lists create by collide. The analyze executable does this on an event-by-event basis and it calculates all observables in two passes over the data files. In the first pass analyze determines the centrality class of the collision. This is done by counting the number of reconstructed charged tracks in each event as a measure of the number of particles produced. Of course since *Trajectum* is a simulation detection efficiency is a 100%. However, for comparison with an actual experiment it is important to use the same method to determine the centrality. Because some experiments make certain cuts on measured data and for comparison we must be able to make the same cuts. After the initial determination of the centrality of each event a second pass over the data is made, in which the observables requested by the user are calculated. Of course certain cuts can be made on these observables such as cuts on: transverse momentum, rapdity or pseudorapidity. Since we can also oversample events in collide, the analyze executable takes each events statistical weight into account. After analyze is done, it produces a file in which a summary of the events generated is given. This file can then in turn be passed to the final executable of Trajectum, collect.

3.6 Collect

Collect is the final step in the *Trajectum* framework. Collect determines the boundaries of the centrality classes and computes the observables from the summaries. This results in a ‘filename.mathematica‘ file, which can be read into ‘Mathematica‘. Multiple instances of collide and analyze can be run in parallel, collect can process all these files at once and correctly calculate each events statistical weight within the entire dataset.

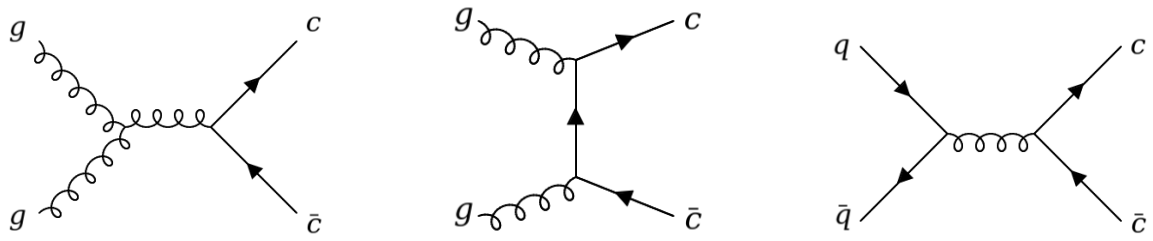

(a) $gg \rightarrow c\bar{c}$ s-channel (b) $gg \rightarrow c\bar{c}$ t-channel (c) $q\bar{q} \rightarrow c\bar{c}$ s-channel

Figure 10: Hard processes for open charm production used in Trajectum

4 Methods

The goal of this work is to research charmed hadron production in different collision systems and the propagation of charm quarks through the QGP medium. To research this we try to recreate different collision systems to look at the difference in charm production for different collision systems. We also explore the different hadronization mechanisms of charm quarks and their impact on the anisotropic flow and transverse momentum spectra of charmed hadrons. To investigate the propagation of charm quarks trough the QGP medium the effect of the spatial charm quark diffusion constant D_s on both anisotropic flow and transverse momentum is investigated. Throughout this entire work, 15000 events are simulated per parametrization and peripheral events are oversampled.
In this section the different simulation methods to tune model parameters on data will be discussed. At first the fragmentation methods deployed within *Trajectum* will be discussed by recreating a pp collision environment. Subsequently the QGP drag force will be turned on and heavy quark diffusion effects as discussed in section (2.5) will be taken into account. Then the impact of coalescence without the presence of heavy quark diffusion within the QGP will be discussed. Finally all elements will be implemented and the implementation of a Pb-Pb collision simulation with a hybrid hadronization approach and heavy quark diffusion will be discussed. In this thesis the behaviour of the charm quark is studied. This study can be extended to also include bottom quarks, but certain model parameters will have to be tuned to measurements of bottom hadrons which are less abundant than charmed hadron measurements.

4.1 proton-proton collision

To simulate a proton-proton collision *Trajectum* uses both Pythia 8.309 [81] and LHAPDF-6.5.4 [82] to calculate the initial momenta and coordinates of the charm quarks produced from the Parton Distribution function (PDF) of the incoming protons. The Pythia settings used for the creation of charm quarks are:

- ("HardQCD:hardccbar = on"), this produces the charm quarks through the $gg \rightarrow c\bar{c}$ and $q\bar{q} \rightarrow c\bar{c}$ channels shown in Fig. 10.
- ("BeamRemnants:primordialkT = on"), this adds the primordial momentum of the parent quarks to the heavy quarks.
- ("4:m0 = 1.275"), to change the charm quark mass from the default value of 1.5 GeV to the 1.275 GeV mass used throughout the *Trajectum* framework.

The beam energy is set to $\sqrt{s_{NN}} = 5.02$ TeV and the PDF used is the default NNPDF2.3 QCD+QED LO [83] for proton beams. The charm quarks are produced through the hard QCD processes shown in Fig. 10. The number of charm quarks produced per binary collision are sampled with a Poisson

H_c	$f(c \to H_c)[\%]$
D^0	$39.1 \pm 1.7(\text{stat})^{+2.5}_{-3.7}(\text{syst})$
D^+	$17.3 \pm 1.8(\text{stat})^{+1.7}_{-2.1}(\text{syst})$
D_s^+	$7.3 \pm 1.0(\text{stat})^{+1.9}_{-1.1}(\text{syst})$
Λ_c^+	$20.4 \pm 1.3(\text{stat})^{+1.6}_{-2.2}(\text{syst})$
Ξ_c^0	$8.0 \pm 1.2(\text{stat})^{+2.5}_{-2.4}(\text{syst})$
D^{*+}	$15.5 \pm 1.2(\text{stat})^{+4.1}_{-1.9}(\text{syst})$

Table 2: Charm quark fragmentation fractions into charm hadrons, $f(c \to H_c)$. Taken from Ref [84]. The fragmentation fractions are determined from measurements in pp collisions at $\sqrt{s} = 5.02$ TeV.

distribution. The average of the Poisson distribution is a model parameter which we can tune, the $c\bar{c}$-rate. All charm quarks produced are back to back charm anticharm pairs. We assume that there is no QGP production in a pp collision. So to simulate this environment we turn off charm quark diffusion and make it impossible for the heavy quarks to hadronize through a coalescence mechanism. This entails that all produced charm quarks hadronize through fragmentation. Heavy quark hadronization in *Trajectum* occurs when the temperature of a fluid cell within the QGP drops down below a predetermined freeze-out temperature T_c. However, as mentioned earlier in proton-proton collisions there is no QGP production. The way this is corrected without uprooting the entire *Trajectum* framework is by making the QGP transparent for heavy quarks so they do not experience any of the effects exerted by the QGP such as heavy quark diffusion. So when the temperature of the QGP fluid cell containing a heavy quark drops below T_c in the case of a proton-proton collision it will fragment into a hadron. There are of course a multiple hadron species a charm quark can fragment into. To determine which hadron species the charm quark will fragment to, we took the fragmentation fractions for open charm hadrons from Ref [84] shown in Table 2. These fragmentation fractions are then summed and normalised in the following way:

$$P_i = \sum_{i=1}^{N_{H_c}-1} f_i(c \to H_c) + f_{i-1}(c \to H_c), \quad P_{tot} = P_{(N_{H_c}-1)},$$
$$P_j = \delta_{ij} \frac{P_i}{P_{tot}}. \tag{4.1}$$

This creates a probability interval between 0 and 1, so the probability of finding a particle species to hadronize to is always one.

In *Trajectum* the fragmentation function used is the Peterson fragmentation function (2.41), [56]. The exact function used is:

$$D(z) = 4\epsilon_c \frac{1}{z}\left(1 - 1/z - \frac{\epsilon_c}{1-z}\right)^{-2}. \tag{4.2}$$

The prefactor of $4\epsilon_c$ is to make sure $D_{max}(z) = 1$ so it can be used as a probability density. The way fragmentation is implemented into *Trajectum* is as follows:

- A random $z' \in [0, 1]$ is generated and plugged into (4.2).
- Another random number $x \in [0, 1]$ is generated and if $x < D(z')$, z' will become the fraction of momentum from the heavy quark carried by the fragmented hadron, so $z' \to z, p_H = zp_Q$.
- However, if $x > D(z')$ another value for both z' and x will be generated and the described process will be repeated until a suitable momentum fraction is found.

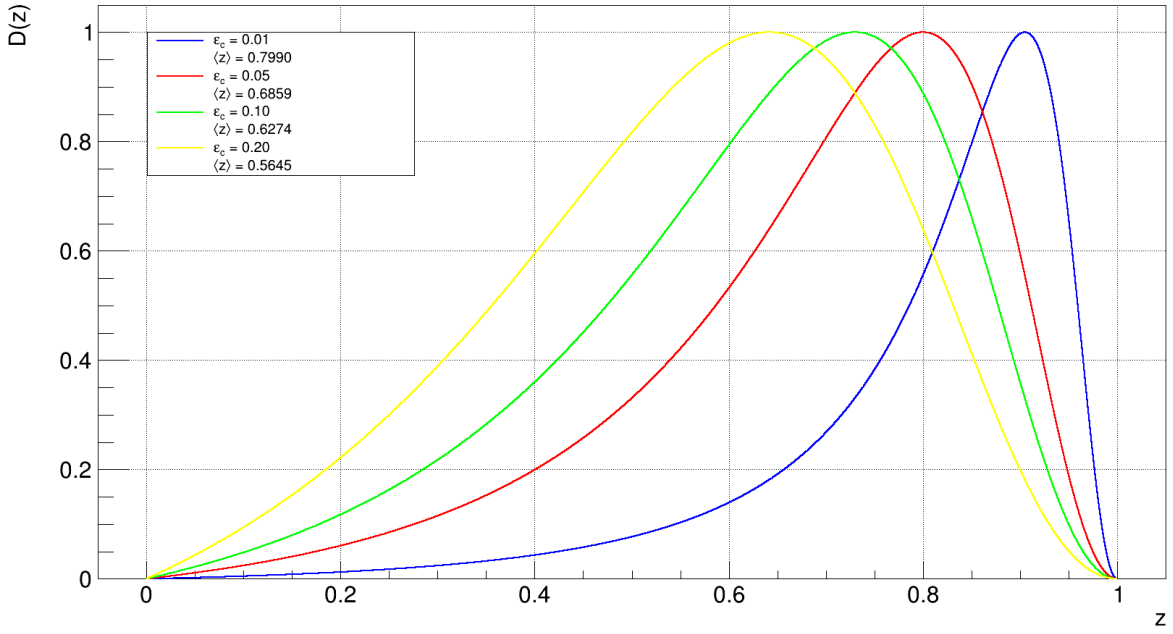

Figure 11: Visualization of the Peterson fragmentation function and the dependence of the average value of the momentum fraction on ϵ_c

Since $D_{max}(z) = 1$ a momentum fraction will always be found. However, there are kinematical constraints implemented in *Trajectum* which makes sure energy conservation is not violated. So if $E_H > E_Q$ the charm quark will be rejected from fragmentation. In equation (4.2) there is one parameter that can be tuned to fit the shape p_{T}-differential cross-sections or multiplicities measured in collision experiments, ϵ_c. The ϵ_c parameter only influences the shape of the p_{T}-differential multiplicities, the number of produced charm quarks in *Trajectum* are governed by the $c\bar{c}$-rate. Fig. 11 shows the ϵ_c dependence of (4.2). In the legend of this figure the average value of z is also shown. This is calculated by this equation:

$$\langle z \rangle = \frac{\int_0^1 zD(z)dz}{\int_0^1 D(z)dz}. \tag{4.3}$$

From Fig. 11 it becomes unequivocally obvious that a smaller value for ϵ_c leads to a larger value of $\langle z \rangle$, meaning that the fragmentation function becomes harder as ϵ becomes smaller. So a smaller ϵ_c leads to more momentum retention of the fragmented hadron from the parent heavy quark than a larger ϵ_c value. Typical values for ϵ_c used in literature are around $\epsilon_c \approx 0.022$ [85].

4.2 Charm Quark interaction with the QGP medium

After recreating a pp collision environment, we investigate the effect of the interactions of charm quarks with the QGP medium. All initial conditions will be kept the same as in the previous section and all charm quarks still only hadronize through fragmentation. The only change we make is that the charm quarks can now interact with the QGP medium.

As discussed in section 2.5, charm quarks lose energy when traversing the QGP due to in-medium interactions. In this subsection the numerical framework used for the in-medium evolution of charm quarks coupled with the expanding QGP will be described. Since a charm quark is considered heavy, gluon radiation is neglected. As mentioned in section 2.5, the spatial diffusion constant scaled with

the thermal wavelength conveniently encodes all relevant components within the Langevin approach for the in-medium interactions of the charm quarks: diffusion and drag. In this work we model the spatial diffusion constant with a linear temperature dependence as is also done in Ref. [86]:

$$2\pi T D_s = \alpha\Big(\frac{T}{T_c} - 1\Big) + \beta, \tag{4.4}$$

the dimensionless parameters α and β will be explored in a wide range to see their impact on the p_{T}-differential multiplicity spectra and the anisotropic flow of charmed hadrons. The parameter α represents the slope of the spatial diffusion constant and β represents the value of $(2\pi T D_s)$ at $T = T_c$. The charm quark motion follows the modified Langevin transport equation (2.33), the relativistic hydrodynamics model supplies the local temperature and flow velocity at the local rest frame of the fluid cell. The numerical procedure to calculate the heavy quark motion in the QGP medium is as follows:

1. The charm quarks are sampled with their initial positions x^μ and momenta p^μ in the laboratory frame, according to their initial phase-space configurations generated by PYTHIA.

2. Then all charm quarks are moved from $\tau \approx 0$ to τ_{fs} as free streaming particles, and their positions x^μ are modified accordingly.

3. Subsequently a QGP fluid cell at x^μ is searched, and both its temperature T and fluid velocity u^μ is extracted from the hydrodynamic simulation. After this the charm quark is boosted to the local rest frame of the fluid cell and the charm quark momentum is calculated in this frame.

4. Make a discrete timestep $\Delta t = \gamma \Delta\tau$, with gamma the Lorentz factor to boost from the laboratory frame to the local rest frame. This timestep is used to update the charm quark momentum p^μ.

$$p_i(t + \Delta t) - p_i(t) = \Big(F_i^{\mathrm{Drag}} + F_i^{\mathrm{Diff}}\Big)\Delta t, \tag{4.5}$$

   the drag and diffusion force terms are driven by the following:

   (a) the drag force term is driven by the drag coefficient η_D, which is related to the spatial and momentum diffusion coefficients D_s and κ in the zero-momentum limit by:

$$\eta_D = \frac{1}{2\pi T D_s}\frac{2\pi T^2}{m_Q}, \quad \kappa = \frac{1}{2\pi T D_s} 4\pi T^3. \tag{4.6}$$

   In *Trajectum* the drag force term is given by:

$$F_i^{\mathrm{Drag}}\Delta t = \exp\Big(\frac{-\gamma \Delta\tau \kappa}{2 m_Q T}\Big) = \exp(-\eta_D \Delta t). \tag{4.7}$$

   (b) the thermal force exerted on the charm quark is driven by the correlation profile given in equation (2.35). This is discretized in the following way:

$$\Big\langle F_i^{\mathrm{Diff}}(t) F_j^{\mathrm{Diff}}(t + n\Delta t)\Big\rangle \equiv \frac{\kappa}{\Delta t}\delta_{ij}\delta_{0n}. \tag{4.8}$$

   This correlation is implemented by sampling a momentum deflection from a normal distribution with width $\sqrt{\kappa/\Delta t}$ using a Box Muller sampling technique [87].

5. When the momentum of the charm quark has been updated its position also gets updated after time step Δt

$$x_i(t + \Delta t) - x_i(t) = \frac{p_i(t)}{E_{p_i}(t)}\Delta t, \tag{4.9}$$

   with p_i the four-momentum obtained in the previous step. After both the momentum and position of the charm quark have been updated in the local fluid rest frame the charm quark is boosted back to the laboratory frame.

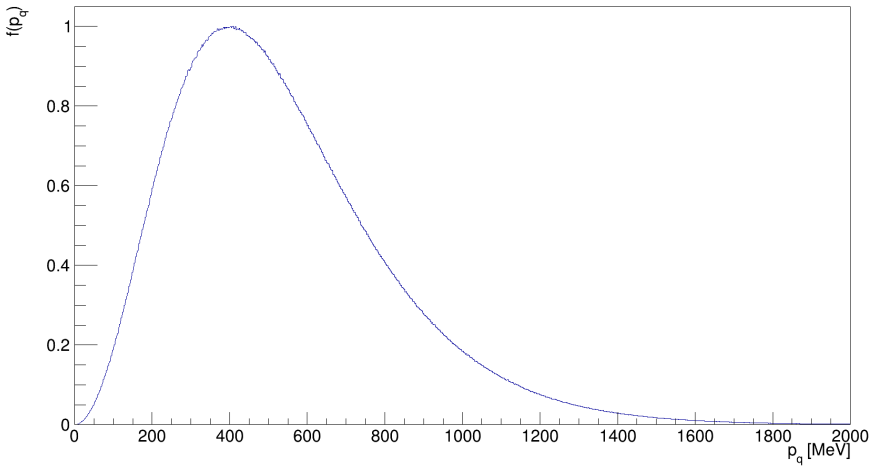

Figure 12: Momentum distribution from which thermal quarks are sampled.

6. Steps (3)-(5) are repeated until the temperature within the local fluid cell drops below the freeze-out temperature, i.e., $T < T_c$ and the charm quark hadronizes.

As can be seen from equations (4.6, 4.7 and 4.8), a larger value for the spatial diffusion constant ($2\pi TD_s$) leads to less drag and less momentum diffusion. This suggests that higher values for the spatial diffusion constant will lead to more suppression of transverse momentum and more collective behaviour.

4.3 Coalescence Implementation

When the temperature within a fluid cell containing a charm quark drops below the freeze-out temperature, $T < T_c$, the charm quark will hadronize. Up until this point we only allowed charm quarks to hadronize through fragmentation. However, charm quarks can hadronize through both fragmentation and coalescence as discussed in section 2.6.2. To purely research the effect of the addition of the coalescence mechanism on top of the fragmentation mechanism, interactions of charm quarks with the medium was turned off.

The probability of a charm quark to hadronize through either fragmentation or coalescence is dependent on its momentum among other things. The most important constraint implemented in this work is that when a quarks momentum goes to zero it is forced to hadronize through coalescence:

$$\lim_{p_Q \to 0} P^{\text{tot}}_{\text{coal}}(p_Q) = 1. \tag{4.10}$$

Where $P^{\text{tot}}_{\text{coal}}$ is the total coalescence probability for a charm quark to either coalesce into a meson or a baryon. All charm quarks must hadronize, since quarks have to be bound, so $P^{\text{tot}}_{\text{coal}}(p_Q) + P_{\text{frag}} = 1$. The probability for a charm quark to coalesce is also dependent on the width parameter of the recombined hadron $\sigma \equiv \sqrt{\mu\omega}$, as was discussed in section 2.6.2. In *Trajectum* the effective thermal mass is the same for all plasma quarks and it is a model parameter which can be tuned, the harmonic oscillator frequency ω is also a model parameter. The way the coalescence probability for mesons and baryons depends on these model parameters is as follows:

$$P^{\text{M}}_{\text{coal}} \propto \frac{N_{DOF}\sigma^3}{9\sqrt{2}}\rho_q, \tag{4.11}$$

$$P^{\text{B}}_{\text{coal}} \propto \frac{N_{DOF}\sigma^6}{27}\rho_q^2. \tag{4.12}$$

Where N_{DOF} are the numbers of degrees of freedom of the produced hadron and ρ_q is the light quark number density calculated by numerically integrating the Fermi-Dirac momentum distribution for the thermal quarks:

$$\frac{g_q}{2\pi^2}\int d^3p \frac{p^2}{e^{E/T_c}+1}. \tag{4.13}$$

However, a charm quark does not necessarily have to recombine with a thermal quark. It can also recombine with another charm quark to form a charmonium state. The probability to form a charmonium state is proportional to:

$$P^{c\bar{c}}_{\text{coal}} \propto \frac{N_{DOF}\sigma^3}{9\sqrt{2}V_{FO}}N_c, \;\; V_{FO} = \frac{4}{3}\pi R^3. \tag{4.14}$$

In this equation the recombinationradius, R is the maximum radius up to which charm quarks can recombine with each other and N_c is the number of charm quarks within this radius. All these probabilities are calculated for all charmed hadron species and added up together, $P^{\text{tot}}_{\text{coal}} = P^{c\bar{c}}_{\text{coal}} + P^{\text{M}}_{\text{coal}} + P^{\text{B}}_{\text{coal}}$. Then to satisfy the limit in equation (4.10), is multiplied with a function dependent on momentum. In this work two different switch functions will be invesigated:

- A Gaussian function, $P^{\text{tot}}_{\text{coal}} \to P^{\text{tot}}_{\text{coal}}\text{exp}\Big(-\frac{p_Q^2}{\chi}\Big)$, $P_{\text{frag}} \to P_{\text{frag}}\Big(1-\text{exp}\Big(-\frac{p_Q^2}{\chi}\Big)\Big)$.
- An exponential function, $P^{\text{tot}}_{\text{coal}} \to P^{\text{tot}}_{\text{coal}}\text{exp}\Big(-\frac{p_Q}{\chi}\Big)$, $P_{\text{frag}} \to P_{\text{frag}}\Big(1-\text{exp}\Big(-\frac{p_Q}{\chi}\Big)\Big)$.

After the switch function is applied the coalescence and fragmentation probabilities are normalized in such a way that $P^{\text{tot}}_{\text{coal}}(p_Q) + P_{\text{frag}} = 1$. When all probabilities have been normalized to one a random number is generated between 0 and 1 to decide the whether the charm quark will recombine into a meson, baryon or charmonium state or if it will fragment. Since the implementation of fragmentation has already been discussed in section 4.1, this subsection will describe the implementation of the coalescence mechanism into either a meson, baryon or charmonium state. Firstly we recall the basics of the coalescence mechanism, which is that a heavy quark combines with at least one comoving thermal parton from the QGP medium or it combines with another heavy quark adding up their respective momenta to produce a hadron. The way this is implemented within *Trajectum* is as follows:

- To form a meson, a charm quark recombines with one thermal quark from the QGP medium. This thermal quarks momentum is sampled from the momentum distribution shown in Fig. 12. This momentum is then boosted from the local fluid rest frame to the laboratory frame and added to the charm momentum. Then the relative momentum $\vec{q}$ between the thermal quark and the charm quark in the center of mass frame of the composite particle is calculated through equation (2.48). From this relative momentum the probability that the recombined meson is accepted is determined by generating a random number $x \in [0,1]$ and checking if:

  $$x < e^{-q^2\sigma^2}, \tag{4.15}$$

  If this is not the case, the charm quark will not recombine with the thermal quark and the hadronization channel will be reevaluated. When the condition in equation (4.15) is satisfied the meson will be formed.

- To form a baryon, the charm quark needs to recombine with two thermal partons. Both these partons momenta are sampled from the momentum distribution shown in Fig. 12. These momenta then also get boosted from the local fluid rest frame to the laboratory frame. Then first the relative momentum in the center of mass frame of the composite baryon between the combination of two quarks $\vec{q}_1$ is calculated and then the relative momentum of the remaining quark with the combination, $\vec{q}_2$ is calculated through equation (2.50). After this is done the merger

probability of the average of all different combinations is calculated and once again a random number $x \in [0, 1]$ is generated to determine if:

$$x < e^{-(q_1^2+q_2^2)\sigma^2}, \tag{4.16}$$

and just as the meson if this is not true the hadronization channel will be reevaluated. If this statement is true the baryon will be formed.

- For a charmonium state the process is the same as for a meson, except for the fact that it recombines with another charm quark so the momentum is already defined in the lab frame.

4.4 Pb-Pb collision

With the implementation of both hybrid hadronization and heavy quark interactions with the QGP medium, a Pb-Pb collision environment can be simulated. The initial creation of the charm quarks from binary nucleon-nucleon collision for the Pb-Pb simulation is similar to that of the pp collision. However, the parton distribution function of a nucleon within a Pb ion is different from the parton distribution of a single proton. So a different LHAPDF file is used, the file used is the EPPS21nlo_CT18Anlo_Pb208/0 PDF [88]. This nuclear parton distribution function takes into account the nuclear effects present in the heavy nuclei, the difference in the initial charm transverse momentum spectra between the different parton distribution functions is shown in Appendix B. The parameters fitted from the pp-collision will now be tested on the Pb-Pb collision simulation and compared to real data.

4.5 Parameter tuning

In summary, at first we recreate a pp-collision environment and tune the input parameters ϵ_c and the $c\bar{c}$-rate on the p_{T}-differential multiplicities ($d^2N/dydp_{\mathrm{T}}$) of open-charmed mesons at midrapidity ($|y| < 0.5$), measured by the ALICE collaboration. Rapidity is defined as:

$$y = \frac{1}{2}\log\Big(\frac{E + p_z}{E - p_z}\Big), \tag{4.17}$$

where E is the particles energy and p_z the particles momentum component along the direction of the beam axis. It is important to note that we model a pp-collision by replacing the nucleon PDF of a nucleon in a Pb ion, with a single proton pdf, turning off all in-medium interactions and only allowing charm quarks to hadronize through fragmentation. However, the entire plasma is still created and evolved in the same way as in a heavy ion collision. To fit the p_{T}-differential multiplicities for open-charmed mesons measured by ALICE, we vary the ϵ_c parameter between 0.015-0.045, to fit the shape of the transverse momentum spectra and we fit the $c\bar{c}$-rate to match the order of magnitude of the data.

Then the contribution of adding in-medium interactions between charm quarks and plasma constituents whilst still forcing charm quarks to hadronize only through fragmentation to the p_{T}-differential multiplicities will be explored. This is done by varying the α and β parameters which govern the spatial charm diffusion coefficient, $(2\pi TD_s) = \alpha(T/T_c - 1) + \beta$, between 0-8. Furthermore, the effect of in-medium interactions on the collective behaviour of open-charmed mesons is explored by looking at the effect of the α and β parameters on the elliptic flow coefficient as a function of transverse momentum $v_2(p_{\mathrm{T}})$ and comparing this to the $v_2(p_{\mathrm{T}})$ of open-charmed mesons measured by ALICE. The elliptic flow coefficients from *Trajectum* are calculated using the reaction-plane method, due to the fact that the reaction plane can be determined perfectly since it is a simulation, but the datapoints measured by ALICE use the scalar product method. Calculation details for the different methods can be found in Ref [89] and Ref [90], for the reaction plane and scalar product method respectively.

Subsequently the effect of adding coalescence as a hadronization mechanism to the pp-collision environment on both the p_{T}-differential multiplicities and $v_2(p_{\mathrm{T}})$ without charm quarks interacting with

the medium is explored. The effects of both switch functions are explored. Finally, a full Pb-Pb collision environment will be simulated by replacing the single proton PDF to the nuclear parton distribution function of a nucleon within a Pb ion taking nuclear effects into account and allowing both in-medium interactions and charm quark hadronization through coalescence. The parameters tuned on the pp-collision environments will then be tested on the Pb-Pb collision environment. Both the p_{T}-differential multiplicities and $v_2(p_{\mathrm{T}})$ measured by ALICE in Pb-Pb collisions at $\sqrt{s_{NN}}$ =5.02 TeV will be compared to the simulation results obtained with the tuned parameters.

5 Results

In this section the results from the collisions simulated by *Trajectum* will be presented and compared to data measured by the ALICE detector. The main two observables presented in this section are: Particle multiplicities at mid-rapidity, $|y| < 0.5$, and elliptic flow in the rapidity range $|y| < 0.8$. This section will be structured as follows: First all QGP and coalescence effects will be turned off to simulate a pp-collision environment where no QGP gets created and all heavy quarks will hadronize through fragmentation; then the impact of heavy quark diffusion will be explored by turning on the QGP drag force; subsequently the effects of coalescence without heavy quark diffusion will be explored; finally a complete Pb-Pb collision with both coalescence and heavy quark diffusion will be simulated and compared to ALICE data.

5.1 pp Results

In this subsection, the results of the p_{T}-differential particle multiplicities ($d^2N/dydp_{\mathrm{T}}$) for prompt D-mesons at midrapidity ($|y| < 0.5$) produced by *Trajectum* from a proton-proton collisions at $\sqrt{s_{NN}} =$ 5.02 TeV are presented. These results are compared to the p_{T}-differential particle multiplicities for prompt D-mesons at midrapidity measured by the ALICE collaboration [14]. For the proton-proton collision simulation all QGP effects are neglected and hadronization is purely through the fragmentation channel. So there are no hadrons produced through coalescence. As discussed in the methods section 4 the fragmentation function used within *Trajectum* is the Peterson fragmentation function (2.41). The only parameter which can be tuned within this fragmentation approach to fix the shape of the p_{T}-differential particle multiplicities to match the measured data is the ϵ_c parameter. To match the exact values of the p_{T}-differential multiplicities the $c\bar{c}$-rate is tuned to $c\bar{c}$-rate = 6. Fig. 13 shows the effect of varying the ϵ_c parameter and a comparison to prompt D^0 meson production from Ref [14]. In this section all symbols representing data points are centered in each p_{T} interval and the horizontal bars represent the bin width. Vertical error bars or bands represent all statistical uncertainties. In the calculation of the model ratios in the lower panel of the left figure of Fig. 13, the uncertainties were propagated treating them as highly correlated. Whilst in the calculation of the ratio between data and model in the bottom panel of the right figure of Fig. 13 the uncertainties were propagated as uncorrelated. This method of uncertainty propagation between ratios is used throughout this entire section.

The effect of the ϵ_c parameter on the p_{T}-differential multiplicities becomes obvious from Fig. 13. Three different values for ϵ_c where used: 0.045, 0.03 and 0.015. A large value for ϵ_c leads to a lower $\langle z \rangle$ than a small value for ϵ_c as can be seen from Fig. 11. As a result the p_{T}-differential multiplicities of the simulations with $\epsilon_c = 0.045$ are largest at low p_{T}, $0 < p_{\mathrm{T}} < 1$ GeV, but for $p_{\mathrm{T}} > 3$ GeV the multiplicities with smaller ϵ_c are larger and vice-versa for the $\epsilon_c = 0.015$ results. The value for ϵ_c which leads to the best agreement with data is $\epsilon_c = 0.03$, which is a reasonable value for the ϵ_c parameter compared to usual literature values [85]. In Fig. 15 the p_{T}-differential multiplicities of D^0, D^+, D^{*+} and D_s^+ are presented and in the bottom panels the ratio between model and data is shown. For all model calculations in Fig. 15 $\epsilon_c = 0.03$. At the intermediate to high p_{T} interval $5 < p_{\mathrm{T}} < 30$ GeV the model predictions for all D meson species presented agree reasonably well. Only for the D^+ meson *Trajectum* overpredicts the p_{T}-differential multiplicity especially in the low transverse momentum region. This is most likely due to the fact that the implementation of fragmentation within *Trajectum* is a form of independent fragmentation, which is subject to large uncertainties when $m_Q \approx p_{\mathrm{T}}$, instead of a more sophisticated approach such as string fragmentation. For baryons the model predictions do not agree very well with the measured data. Fig. 14 shows both the p_{T}-differential multiplicity of the $\Lambda_c^{\pm}$ baryon and the ratio between the $\Lambda_c^{\pm}$ and D^0 p_{T}-differential multiplicities. From these figures it becomes exceedingly obvious that the simple implementation of independent fragmentation is not equipped to accurately predict baryon formation. The right hand side of Fig. 14 shows the p_{T}-dependence of the $\Lambda_c^{\pm}/D^0$ multiplicity ratio. In the datapoints taken from Ref [91] a clear trend

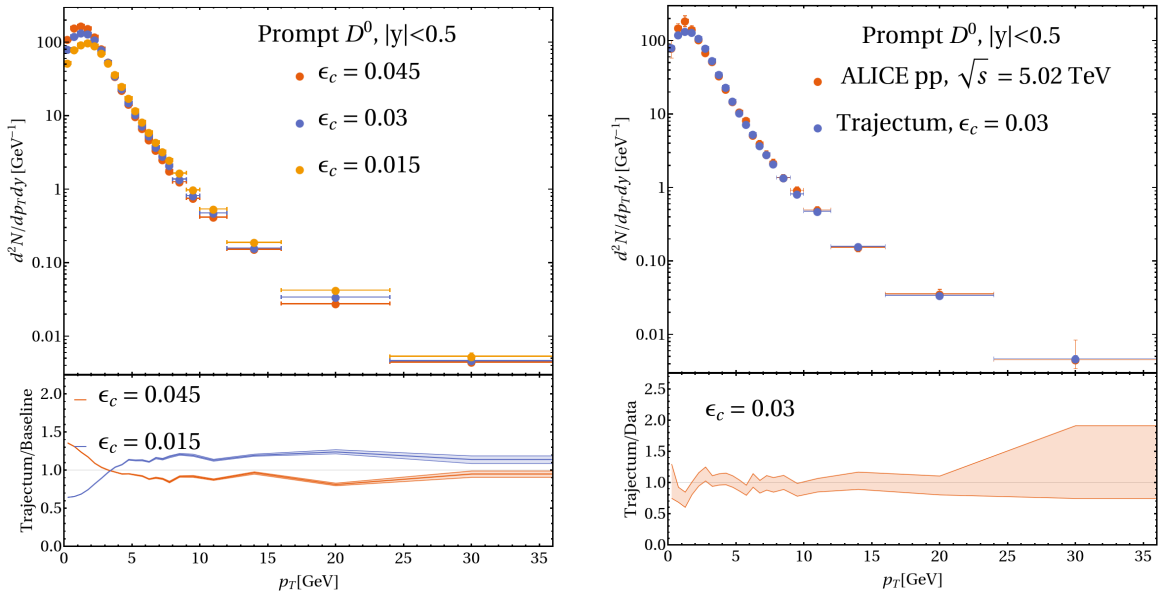

Figure 13: Left: D^0 meson p_{T}-differential multiplicities predicted by *Trajectum* for different values of ϵ_c. The bottom panel shows the ratio of the different model calculations for different values of ϵ_c, the baseline calculation uses $\epsilon_c = 0.03$. Right: Comparison of D^0 meson p_{T}-differential multiplicities calculated by *Trajectum* to the values measured by ALICE. Datapoints taken from [14].

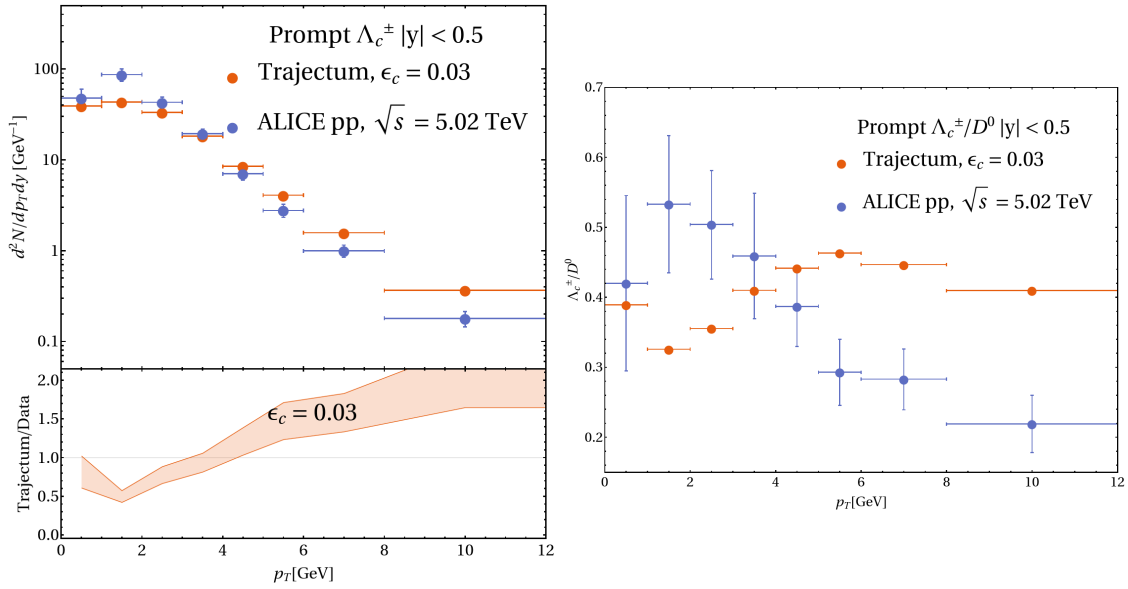

Figure 14: Left: Λ_c baryon p_{T}-differential multiplicity as produced by *Trajectum* compared to the multiplicity measured by ALICE [91]. Right: The ratio of the p_{T}-differential Λ_c multiplicity divided by the D^0 p_{T}-differential multiplicity as produced by *Trajectum* compared to the ratio measured by ALICE [91]

is visible, the ratio peaks at intermediate p_{T} around (1-2) GeV and then gradually decreases with increasing transverse momentum. The ratio produced by *Trajectum* shows no such p_{T} dependence, but rather stays constant around a ratio of 0.4 with small deviations. The only models which have been able to accurately predict these ratios are models which also include color reconnection.

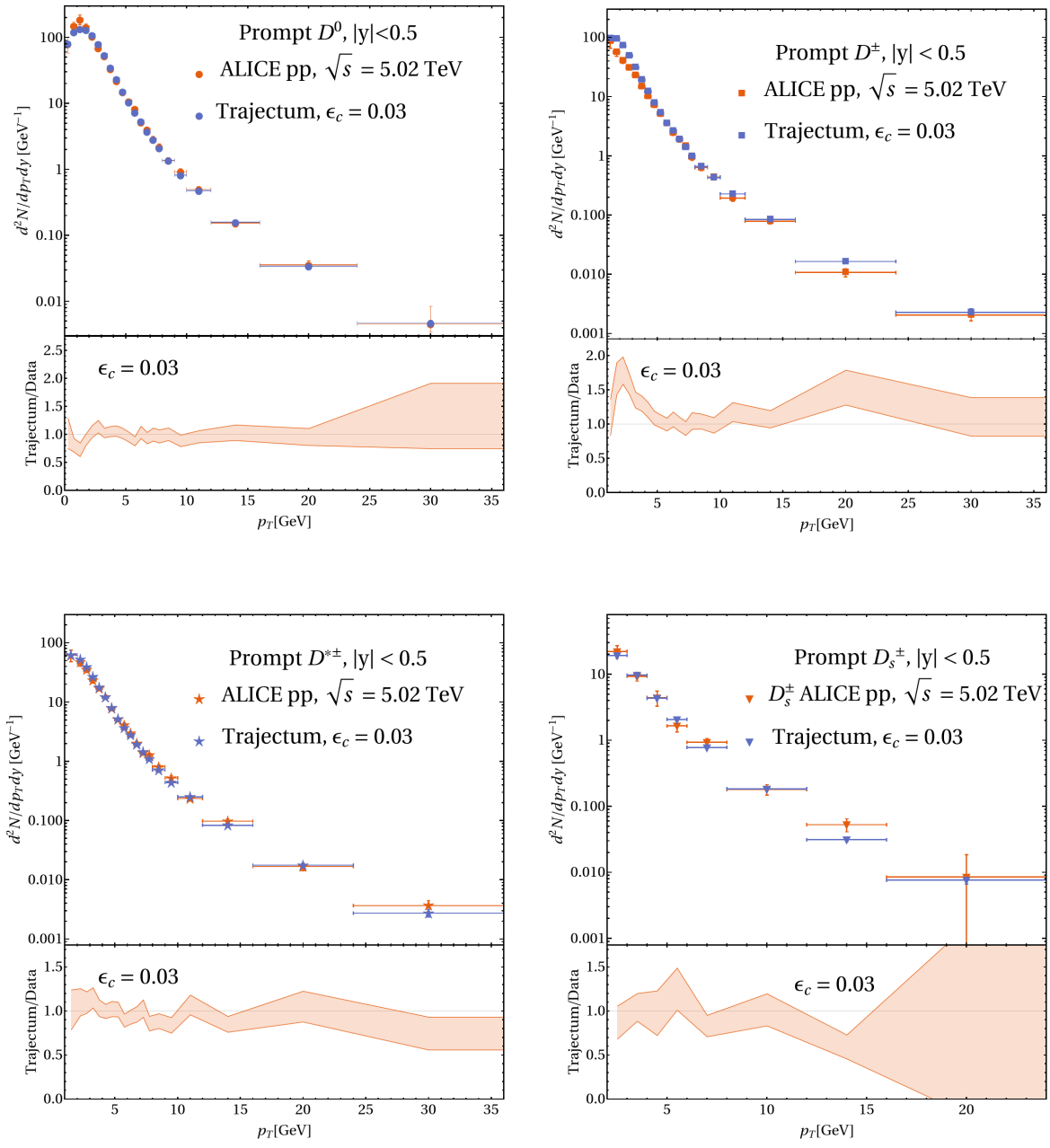

Figure 15: p_{T}-differential multiplicity of all prompt D meson species produced in pp collisions compared to model predictions by *Trajectum* with $\epsilon_c = 0.03$. The ALICE data is taken from Ref [14]. The lower panel of each plot shows the ratio between model predictions and data.

5.2 pp Results with drag force

In this subsection, results of the both p_{T}-differential particle multiplicities ($d^2N/dydp_{\mathrm{T}}$) for prompt D^0-mesons at midrapidity ($|y| < 0.5$) and the average elliptic flow $v_2(p_{\mathrm{T}})$ coefficient for non-strange D-meson species in a rapidity range of $|y| < 0.8$ are presented. These results are obtained from a proton-proton collision simulation with a center-of-mass energy of at $\sqrt{s_{NN}} = 5.02$ TeV, where the produced charm quarks interact with the QGP medium created and all charm quarks hadronize through fragmentation. As mentioned in section 4.5 the plasma is initialised and evolved in the same way as in a heavy-ion collision, but the parton distribution function is that of a free proton instead of a PDF including nuclear effects. The p_{T}-differential multiplicities are compared to the results for a pp-collision environment where there is no in-medium interaction of charm quarks, the baseline model parameters have been fixed to $\epsilon_c = 0.03$ and the $c\bar{c}$ production rate = 6. The parameters varied in this section are the parameters governing the spatial charm quark diffusion constant $(2\pi TD_s) = \alpha(\frac{T}{T_c} - 1) + \beta$.

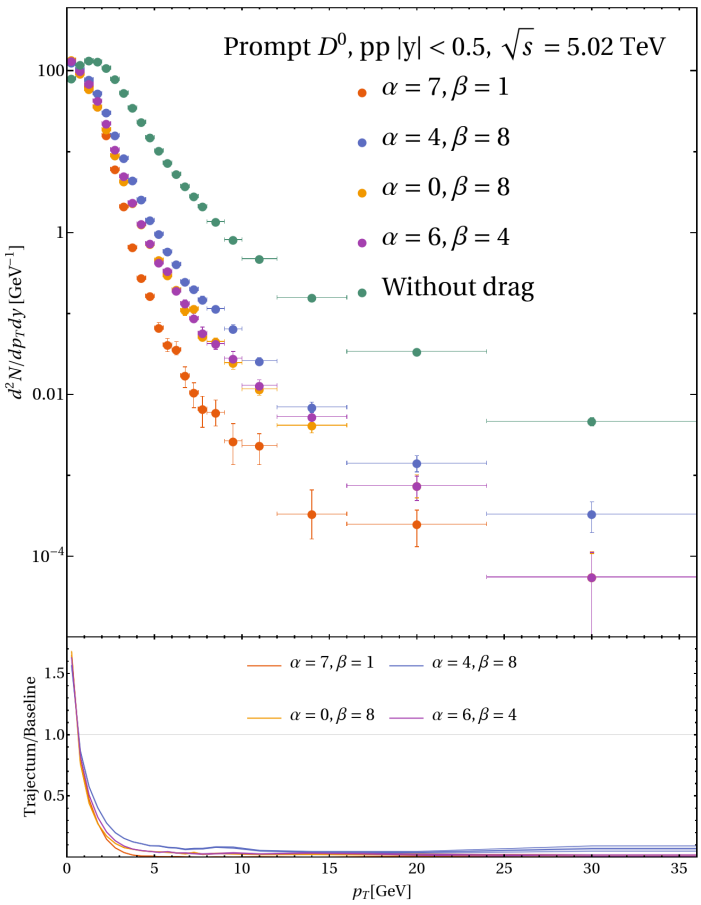

Figure 16: D^0 meson p_{T}-differential multiplicities predicted by *Trajectum* for different values of the spatial charm quark diffusion constant $(2\pi TD_s) = \alpha(\frac{T}{T_c} - 1) + \beta$. The bottom panel shows the ratio of the different model calculations for different values of the spatial charm quark diffusion constant, the baseline calculation assumes no drag and no diffusion with a fragmentation parameter $\epsilon_c = 0.03$.

Fig. 17 shows the p_{T}-differential mulitplicity of D^0 mesons with and without in-medium interactions for different parametrizations of the spatial charm diffusion coefficient. From this figure one thing quickly becomes obvious and that is that a higher value for $(2\pi TD_s)$ leads to a less extreme modification of the transverse momentum distribution. This can be seen from the fact that the parameterization

of $(2\pi TD_s) = 4(\frac{T}{T_c} - 1) + 8$ gives the highest p_{T}-differential multiplicity over the intermediate to high transverse momentum range (1-36) GeV. This is to be expected since the spatial diffusion coefficient is inversely related to the momentum diffusion coefficient, $\kappa = \frac{4\pi T^3}{2\pi TD_s}$. As discussed in section 4 a lower momentum diffusion coefficient will lead to less drag exerted on the charm quark, meaning a less extreme modification of its momentum. Another interesting feature in this figure is that for the value $\alpha = 7$, $\beta = 1$, the modification of the transverse momentum is the most extreme. For this parameterization the p_{T}-differential multiplicity is the lowest throught the intermediate to high transverse momentum range (2-36) GeV. When this parameterization is compared to the parameterization of $\alpha = 0$, $\beta = 8$ it seems that β has a greater influence on the transverse momentum spectrum than α. Since α is the slope of $(2\pi TD_s)$ this could mean that in most events the QGP temperatures vary between 1 to 2 T_c not often exceeding $2T_c$, which is the value at which the two parameterizations give the same value for $(2\pi TD_s)$, due to the vastly different p_{T}-differential momentum spectra for the two paremeterizations.

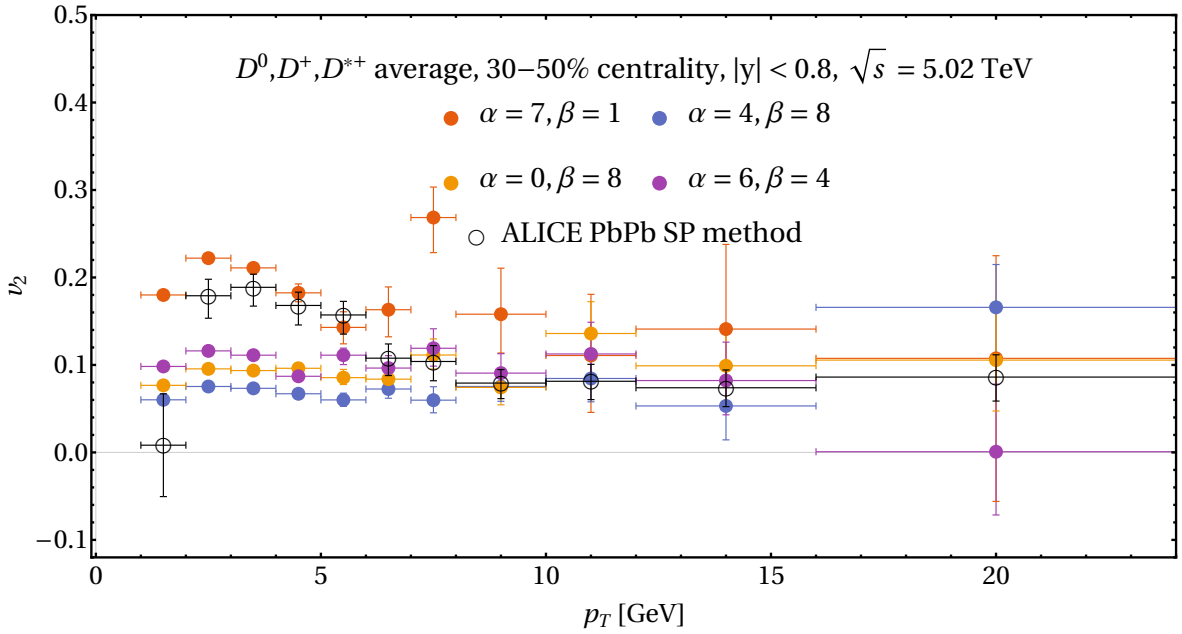

Figure 17: The average elliptic flow coefficient for all non-strange D-meson species as produced by *Trajectum* for different values of the spatial charm quark diffusion coefficient is shown here compared to the average elliptic flow of non-strange D-meson species as measured by ALICE [90].

Fig. 17 shows the average elliptic flow coefficient for non-strange D-meson species in the 30-50% centrality region. In Fig. 17, it can be seen that there is more elliptic flow when the spatial diffusion coefficient is lower. Which is to be expected, since a lower spatial diffusion leads to more momentum diffusion and drag and thus more collective behaviour. The greatest elliptic flow in the low to intermediate transverse momentum region (1-10) GeV is produced by the parameterization where $\alpha = 7$ and $\beta = 1$. This once again suggests that the QGP temperature in most events lies between 1 to 2 T_c. Another interesting feature in this plot is that in the low to intermediate p_{T} region the parameterization where $\alpha = 0$ and $\beta = 8$ consistently has a lower v_2 coefficient than the parameterization where $\alpha = 6$ and $\beta = 4$. This could further constrain the QGP temperature to the region of (1-5/3) T_c, since at $5/3T_c$ both parameterizations take on the same value for $(2\pi TD_s)$ and below that temperature the parameterization where $\alpha = 6$ and $\beta = 4$ leads to a lower $(2\pi TD_s)$. At higher p_{T} the error bars on the v_2 become so large that there can not be any valid conclusions drawn from this region except for the fact that the flow needs to approach zero for high p_{T}.

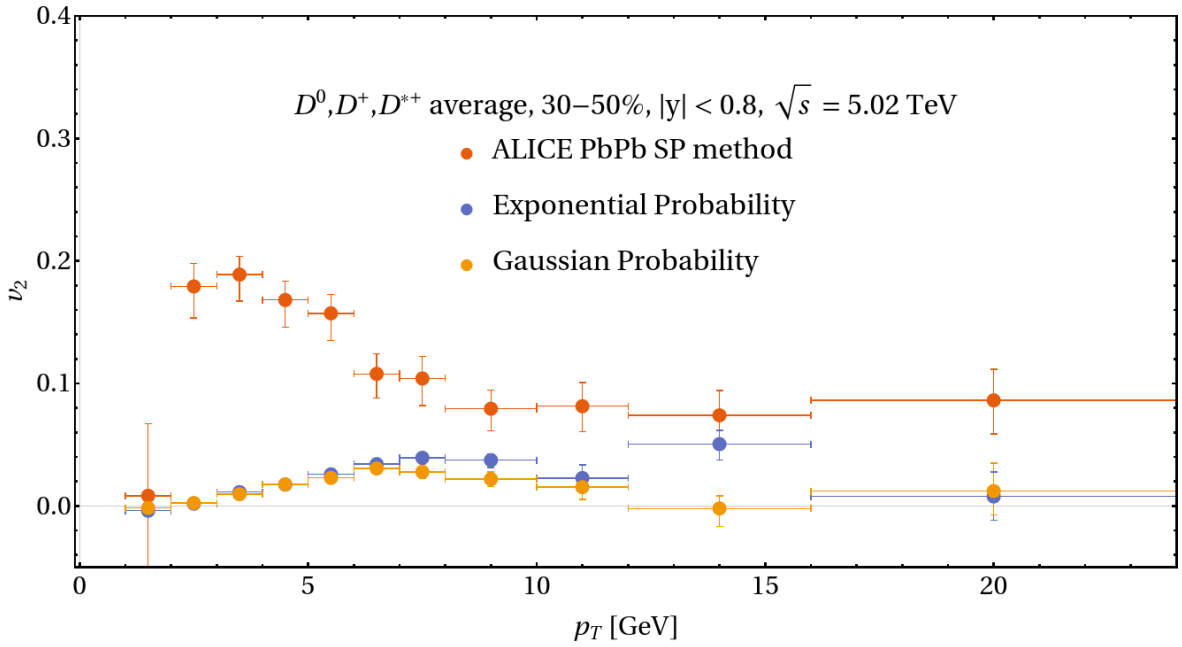

Figure 18: Average elliptic flow ($v_2(p_T)$) coefficients of non-strange D mesons for charm quarks hadronizating through both fragmentation and coalescence. Compared to ALICE v_2 measurements [90]

5.3 pp Results with coalescence

In this subsection, results of the both p_T-differential particle multiplicities ($d^2N/dydp_T$) for prompt D^0-mesons at midrapidity ($|y| < 0.5$) and the average elliptic flow $v_2(p_T)$ coefficient for non-strange D-meson species in a rapidity range of $|y| < 0.8$ are presented. These results are obtained from a proton-proton collision simulation with a center-of-mass energy of at $\sqrt{s_{NN}} = 5.02$ TeV, but charm quarks are now also able to hadronize through coalescence in addition to fragmentation. However, Charm quarks do not interact with the QGP medium. The results for the hybrid hadronization implementation will be compared with the baseline pp-results for purely fragmentation and the elliptic flow will be compared to the elliptic flow measured by ALICE in [90]. Fig. 20 shows the p_T-differential multiplicities for all D-meson species where they can hadronize through both coalescence and fragmentation compared to p_T-differential multiplicity of all D-meson species where hadronization only occurs through fragmentation. From this figure the first thing that becomes clear is that at high transverse momentum ($p_T > 10$ GeV) there are very few charm quarks hadronizing into D-mesons through the coalescence mechanism, which is expected. Another thing that can be seen from this graph is that there is a negligible difference between the gaussian and exponential switch function used. This means that the kinematic constraints through the Wigner functions (2.47, 2.49) is the dominant probability mechanism. At intermediate p_T there is a large spike in all meson multiplicities with respect to the multiplicities where charm quarks only hadronize through fragmentation, with a peak around 5 GeV. Since coalescence combines the momenta of recombining quarks this is also expected behaviour. However, the increase of D_s mesons is very large, of the order of 10 times more D_s mesons produced around 5 GeV. This is lot higher than expected and is probably due to the underestimation of the strange quark thermal mass adopted in Trajectum.

In Fig. 18 the average non-strange elliptic flow coefficients are shown as a function of transverse momentum. Also for the elliptic flow predictions there is negligible difference between the exponential and gaussian switch functions. For both there is some small collective behaviour in the intermediate

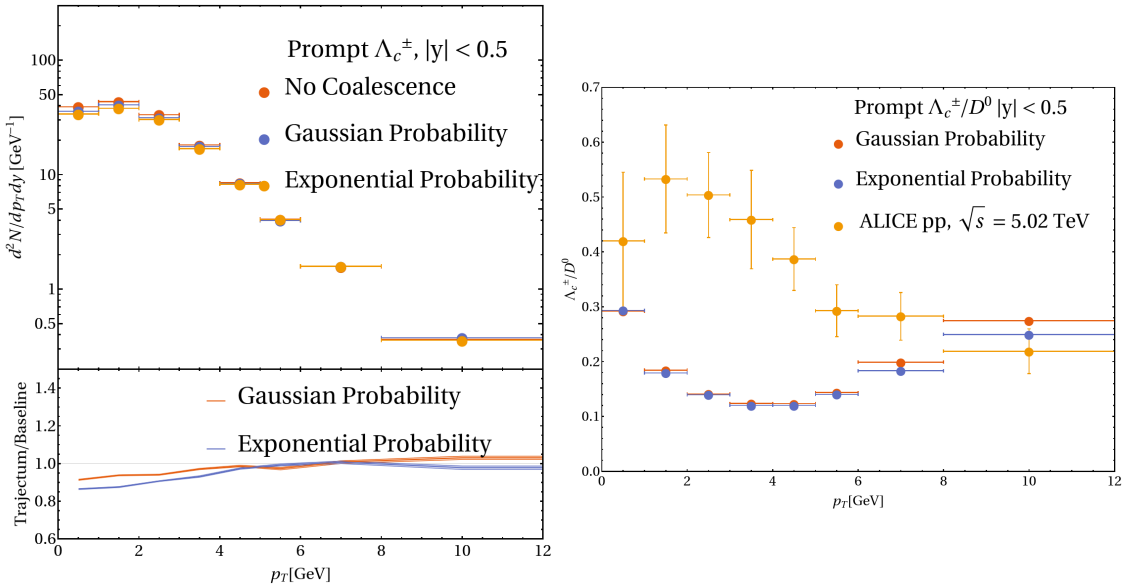

Figure 19: Left: Λ_c baryon p_{T}-differential multiplicity as produced by *Trajectum* through both coalescence and fragmentation compared to the multiplicity of Λ_c baryons produced only through fragmentation. Right: The ratio of the p_{T}-differential Λ_c multiplicity divided by the D^0 p_{T}-differential multiplicity for Λ_c baryons and D^0 mesons produced through both fragmentation and coalescence compared to the baryon to meson ratio through only fragmentation.

p_{T} range (0-10) GeV, but the v_2 for a Pb-Pb collision is expected to be much higher. This leads us to believe that most of the elliptic flow from heavy ion collisions comes from the in-medium interactions of the charm quarks with the constituents of the plasma.
Fig. 19 shows the p_{T}-differential multiplicity of Λ_c baryons through both coalescence and fragmentation compared to the production through fragmentation only. Here something peculiar is happening. At low p_{T} the yield with coalescence is lower than the yield through only fragmentation. A possible explanation for this is an overestimation of the probability for a charm quark to recombine into a D meson, and therefore there are no charm quarks left to recombine into a Λ_c baryon. On the right hand side of this figure the baryon to meson ration of Λ_c/D^0 is shown and compared to the value measured by ALICE [90]. This figure shows that the ratio of Λ_c/D^0 produced by *Trajectum* goes down at intermediate p_{T} instead of going up as is shown in the measured data. This confirms that in this transverse momentum range the probability to recombine into a D meson as opposed to a Λ_c baryon is too high.

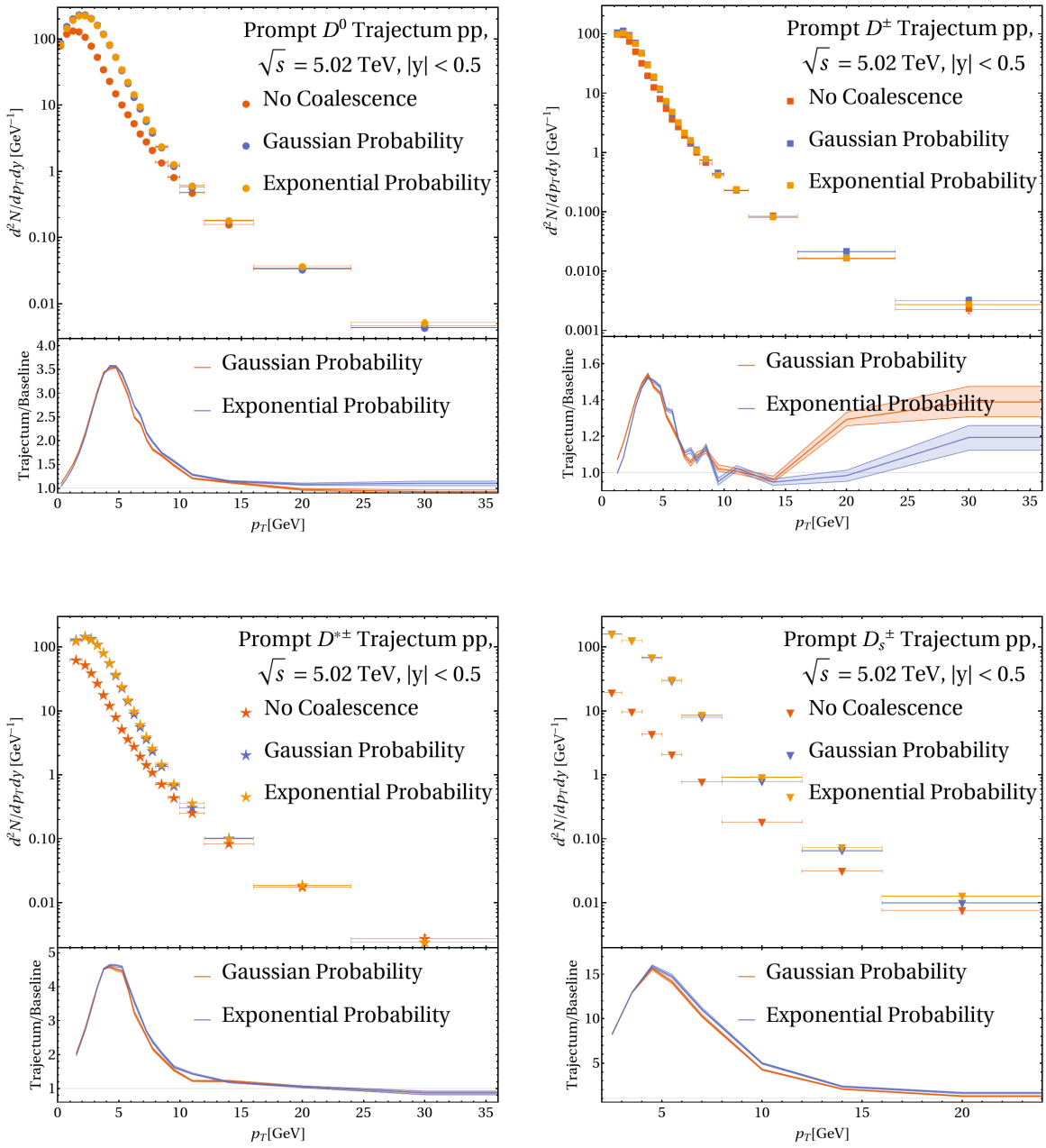

Figure 20: p_{T}-differential multiplicity of all prompt D meson species produced through both coalescence in fragmentation in pp collisions compared to model predictions by *Trajectum* with hadronization only through fragmentation and $\epsilon_c = 0.03$. The lower panel of each plot shows the ratio between the model predictions with and without coalescence.

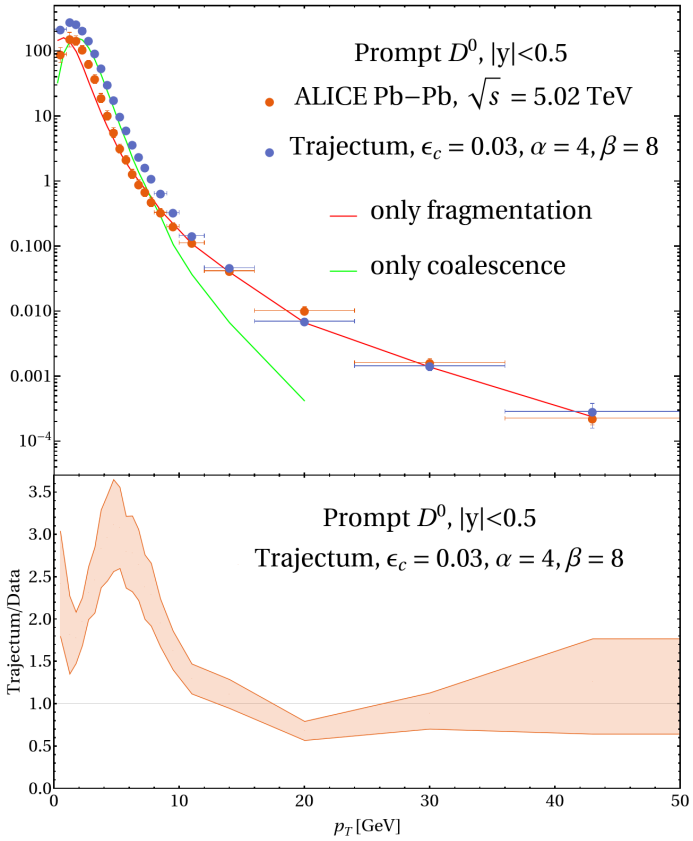

Figure 21: The p_{T}-differential yields of prompt D^0 mesons as produced by *Trajectum*, compared to the p_{T}-differential yields measured by ALICE [92]. The red line shows the D^0 mesons which hadronized through fragmentation and the green line shows the D^0 mesons which hadronized through coalescence.

5.4 Pb-Pb Results

In this section, we present the result of a full Pb-Pb simulation. This means that charm quarks can hadronize through both coalescence and fragmentation, and the charm quarks interact with the constituents of the QGP medium. Also, the free proton PDF is replaced by a nuclear parton distribution function for a ^{208}Pb nucleus, which takes nuclear effects into account. Results of both the p_{T}-differential particle multiplicities ($d^2N/dydp_{\mathrm{T}}$) for prompt non-strange D-mesons at midrapidity ($|y| < 0.5$) and the average elliptic flow $v_2(p_{\mathrm{T}})$ coefficient for non-strange D-meson species in a rapidity range of $|y| < 0.8$ are presented. The p_{T}-differential particle yields and elliptic flow coefficients obtained by *Trajectum*, will be compared to the yields and elliptic flow coefficients measured by the ALICE collaboration [92] and [84] respectively. The ϵ_c parameter has been fixed to $\epsilon_c = 0.33$, since this was the best fit to the pp collision data. The parameters α and β governing the spatial diffusion constant are fixed to $\alpha = 4$ and $\beta = 8$ throughout this section.

Fig. 21 shows the p_{T}-differential multiplicities for D^0 mesons and the contributions of the different hadronization mechanisms. The green line represents the amount of D^0 mesons which have hadronized through coalescence and the red line shows the number of D^0 mesons which have hadronized through fragmentation. From this figure the hierarchy between the two different hadronization mechanisms be-

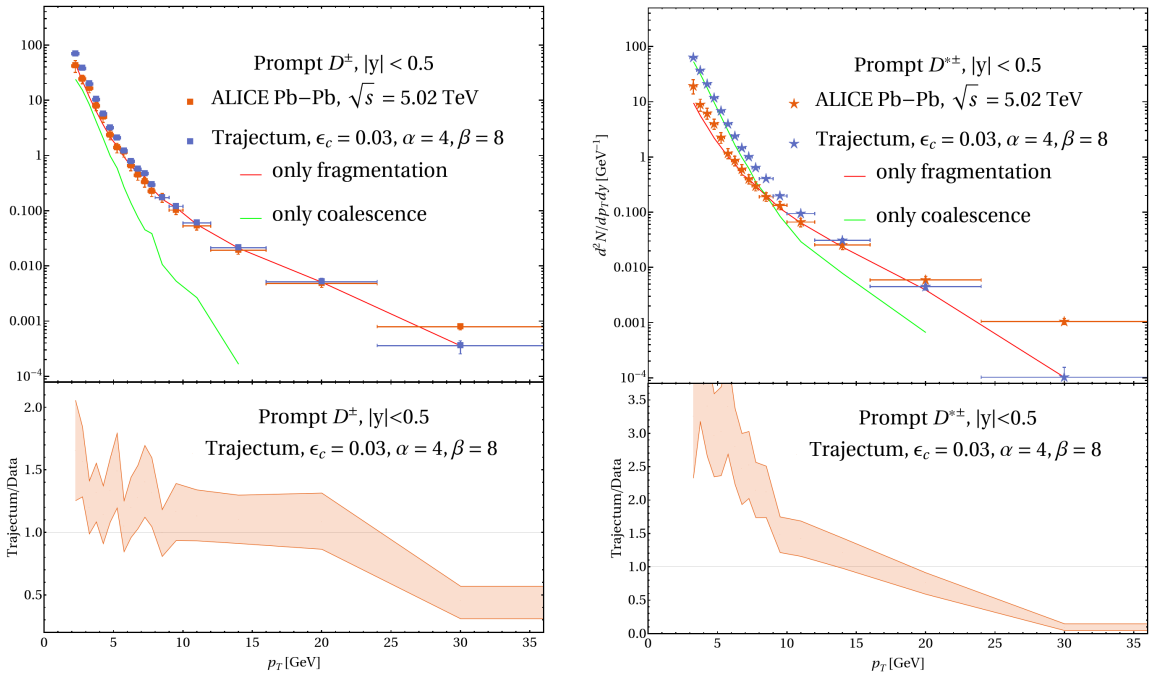

Figure 22: Left: prompt $D^{\pm}$ meson p_{T}-differential multiplicities predicted by *Trajectum*. Right: prompt $D^{*\pm}$ meson p_{T}-differential multiplicities predicted by *Trajectum*. Both p_{T}-differential meson yields are compared to the prompt D-meson yields measured by ALICE [92] in Pb-Pb collisions at $\sqrt{s_{NN}} = 5.02$ TeV. The green lines show the D-mesons hadronized through coalescence and the red lines represent the D-mesons hadronized through fragmentation.

comes clear. At intermediate transverse momentum (2-8) GeV, the dominant production mechanism is coalescence. At higher p_{T} fragmentation rapidly becomes the favoured hadronization mechanism. So much so that at a transverse momentum of over 14 GeV the contribution of coalescence to the p_{T}-differential multiplicity can be considered negligible. So at low transverse momentum most charm quarks hadronize through coalescence and at high transverse momentum the preferred hadronization mechanism for charm quarks is fragmentation, as expected. The p_{T}-differential multiplicity for D^0 mesons is overestimated in the region where coalescence is the dominant mechanism. At higher transverse momentum ($p_{\mathrm{T}} > 10$) GeV the predictions by *Trajectum* agree reasonably well with the data. In Fig. 22 the p_{T}-differential yields for the other two non-strange D-meson species are shown. In this figure the predictions for the $D^{\pm}$ mesons agree reasonably well with the measured data over the transverse momentum region (2-24) GeV. However, the predictions for the $D^{*\pm}$ mesons do not agree with the data in any part of the transverse momentum region.

Fig. 23 and Fig. 24 show the elliptic flow coefficients of non-strange D mesons as a function of transverse momentum. In the 0-10% centrality interval it can be seen already that at low to intermediate p_{T} (0-10) GeV *Trajectum* under predicts the elliptic flow of non-strange D mesons. The under prediction of elliptic flow at low to intermediate transverse momentum becomes even more obvious in the 30-50% centrality region. In the elliptic flow measurements by ALICE [84] there is a pronounced peak around $p_{\mathrm{T}} \approx 3$ GeV, which is absent in the model predictions by *Trajectum*. Since the elliptic flow is mostly driven by the in-medium interaction of charm quarks this suggests that a different parameterization for the temperature dependence of the spatial diffusion coefficient and/or a momentum dependence in

the spatial diffusion coefficient is needed to correctly predict the elliptic flow.

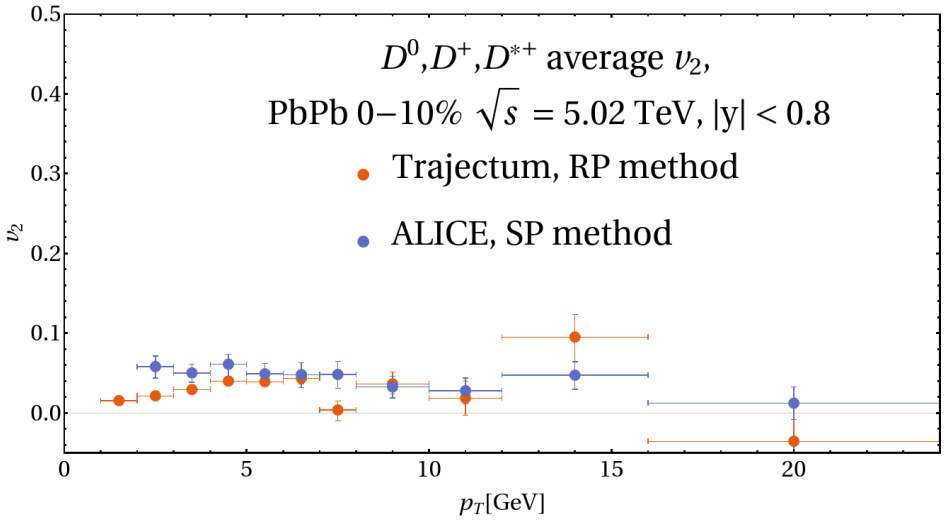

Figure 23: The average $v_2(p_T)$ of non-strange D mesons at 0-10% centrality predicted by *Trajectum* compared to the measured elliptic flow coefficients by ALICE [84]

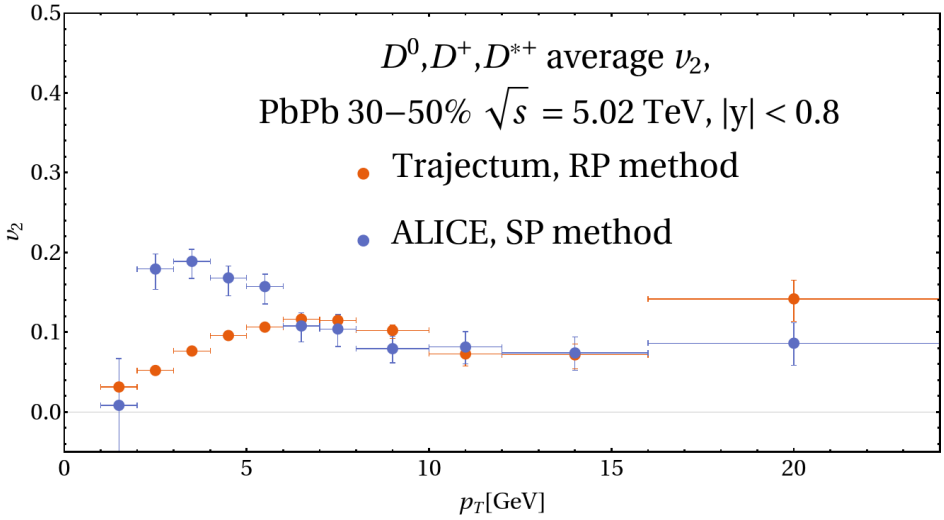

Figure 24: The average $v_2(p_T)$ of non-strange D mesons at 30-50% centrality predicted by *Trajectum* compared to the measured elliptic flow coefficients by ALICE [84]

6 Summary and Conclusion

In this section the results of the conducted research will be summarised. The next section discusses the conducted research and gives an outluk on potential future research which can be done based on this work.

In this work the production of open charmed hadrons was investigated using the *Trajectum* theoretical framework. These results were obtained by firstly recreating a pp collision environment and from there building up to a Pb-Pb collision environment. This was done by individually adding in in-medium interactions between charm quarks and the constituents of the hot and dense plasma and adding the option of hadronization through coalescence as a mechanism to form a hadron. Finally a nuclear PDF was added to the calculations to also include nuclear effects in the simulation.

The p_{T}-differential multiplicies of D mesons at midrapitity at a collision energy of $\sqrt{s_{NN}} = 5.02$ TeV were calculated using the Peterson fragmentation function with the ϵ_c parameter set to $\epsilon_c = 0.33$. It was found that this value for the ϵ_c parameter leads to good agreement with the measured data for D mesons. However, this independent fragmentation calculation was not able to correctly reproduce the $\Lambda_c^{\pm}$ transverse momentum spectrum and the $\Lambda_c^{\pm}/D^0$ baryon to meson ratio.
For the simulations of the p_{T}-differential multiplicies of D mesons and the elliptic flow with the inclusion of in-medium interactions between the charm quarks and the QGP. It was found that the value of the charm quark diffusion constant at the critical temperature $T = T_c$ was the dominant parameter in comparison to the slope of the linear diffusion constant. In other words, for the linear temperature dependence assumption of the charm quark diffusion constant $(2\pi T D_s) = \alpha(T/T_c - 1) + \beta$, β has more influence on both the p_{T}-differential yield and the elliptic flow of D mesons than α.
For the simulations with the inclusion of coalescence as a hadronization mechanism, it was found that the difference in the switch function chosen to influence the transition from coalescence to fragmentation as outlined in equations (4.3) was negligible. This shows that the Wigner function (2.47) for a given meson is dominant in picking the hadronization mechanism. Furthermore, it was shown that the addition of coalescence as a particle production mechanism had limited effects on the elliptic flow of the produced non-strange D mesons.
The simulation of the full Pb-Pb collision environment showed an under prediction of the elliptic flow at low to intermediate transverse momentum. The p_{T}-differential yield of $D^{\pm}$ mesons showed reasonable agreement with data. However, both D^0 and $D^{*\pm}$ mesons showed differences in the predicted p_{T}-differential yields and the measured yields by the ALICE collaboration. To make more accurate predictions using *Trajectum*, further research is needed. The next section includes suggestions for further research based upon this work.

7 Discussion and Outlook

The results for the open charmed hadron production in heavy-ion collisions as simulated by the *Trajectum* framework were presented in this work. In this secion the steps which can be taken in further research based on this work to further increase the accuracy of the model predictions will be discussed.

The modeled in-medium heavy quark energy loss was only through collisional energy loss in this work. However, at LHC energies the heavy quarks themselves become ultra-relativistic [45] and radiative energy loss through gluon radiation becomes the dominant effect at high transverse momentum. In Ref [45] the Langevin equation governing the heavy quark energy loss is modified in the following way:

$$\frac{d\vec{p}}{dt} = -\eta_D(p)\vec{p} + \vec{\xi} - \frac{d\vec{p}_g}{dt}, \tag{7.1}$$

where $\vec{p}_g$ is the momentum of the radiated gluon. The medium-induced gluon momentum is calculated from the higher-twist formalism [93]:

$$\frac{dN_g}{dxdk_\perp^2 dt} = \frac{2\alpha_s(k_\perp)\hat{q}}{k_\perp^4} P(x) sin^2\Big(\frac{t-t_i}{2\tau_f}\Big)\Big(\frac{k_\perp^2}{k_\perp^2 + x^2 m_Q^2}\Big), \tag{7.2}$$

where $k_\perp$ is the transverse momentum of the radiated gluon, and x is the ratio of the gluon energy over the heavy quark energy, the gluon splitting function is denoted by $P(x)$, the formation time of the gluon is τ_f and $\hat{q}$ is the gluon transport coefficient which can be related to the spatial diffusion constant. The probability to radiate a gluon during each timestep Δt is then given by the following integral:

$$P_{\text{rad}} = \Delta t \int dxdk_\perp^2 \frac{dN_g}{dxdk_\perp^2 dt}. \tag{7.3}$$

So in addition to the update of the momentum through diffusion and drag in the step by step process shown in 4.2 the gluon radiation should also be included.
A linear temperature dependence of the spatial charm quark diffusion coefficient was assumed. Other works [9] have also explored a quadratic temperature temperature dependence,

$$2\pi T D_s = a + b\Big(\frac{T}{T_c}\Big)^2. \tag{7.4}$$

Testing out different temperature dependencies and their effect on the elliptic flow and p_{T}-differential hadron yields would be an interesting test to constrain the temperature dependence of the spatial diffusion coefficient.

Furthermore, the number of D mesons formed through coalescence by *Trajectum* seems to be influenced by the number of resonances this D meson species has. For further work it would be interesting to implement a way to only include the ground state D meson production and first correctly predict the production of these mesons, before including the resonance mesons. A simple PDG selection is shown in Appendix A.

Another big discrepancy between model predictions and measured data is the p_{T}-differential baryon to meson ratio $\Lambda_c^\pm/D^0$. This is most likely due to the fact that *Trajectum* uses an indepent fragmentation method, which is a little outdated. Recent works using fragmentation through color reconnection such as Pythia 8 (CR Mode 2), have been able to succesfully reproduce the p_{T}-differential $\Lambda_c^\pm/D^0$ ratio [90]. So implementing a more sophisticated fragmentation method would most likely lead to more accurate baryon production through fragmentation.

Within *Trajectum* all thermal quarks, u,d and s, have the same mass of 300 MeV. However, strange quark masses are usually modeled with a mass around 475 MeV [45]. This is a significant increase so

adding a more correct thermal mass for the s quark should lead to more accurate predictions of D_s production.
Also the initial charm quarks in this work are produced using the ("HardQCD:hardccbar = on") setting of Pythia. However, this does not take additional charm production sources such as flavor excitation and shower branchings into account which are major additional sources. This can be circumvented by producing the charm quarks with the SoftQCD group from Pythia.

For further work, it would also be interesting to perform a Bayesian parameter analysis on the parameters governing the production of charmed hadrons in *Trajectum*. In order to further constrain all the model parameters using measured data.

This work still leaves a lot to be improved upon. However, a promising start was made for the further exploration of the production of open charmed hadrons using the *Trajectum* theoretical framework.

8 Acknowledgements

I would like to thank my daily supervisor Olaf. Not only for your always open door and listening ear when I had a problem, but also for the laughs shared during lunch and all the help provided during this year. Also I would like to thank my other supervisor Alessandro, for the help with writing and for the jokes during meetings which always made the days a bit better. Less on the science side I would like to thank everyone from J.C. Beluga for lending a listening ear and a beer when I had to complain about my research. Last but not least I would like to thank my parents and my sister for all the support during this year.

A Appendix

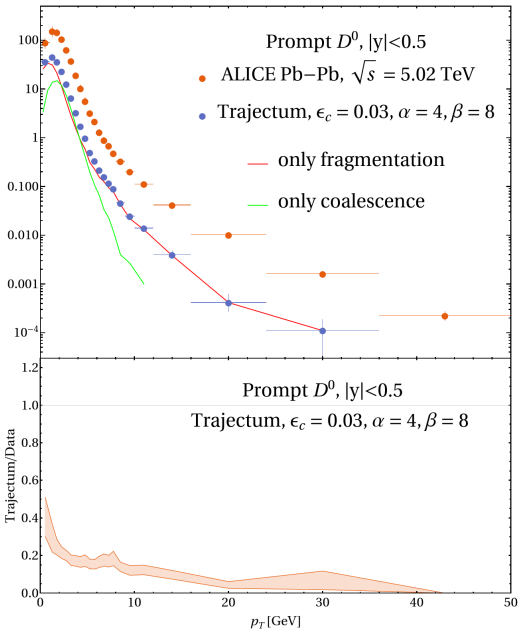

Figure 25: D^0 p_{T}-differential multiplicity with an explicit PDG = 421 selection compared to ALICE measurements [92].

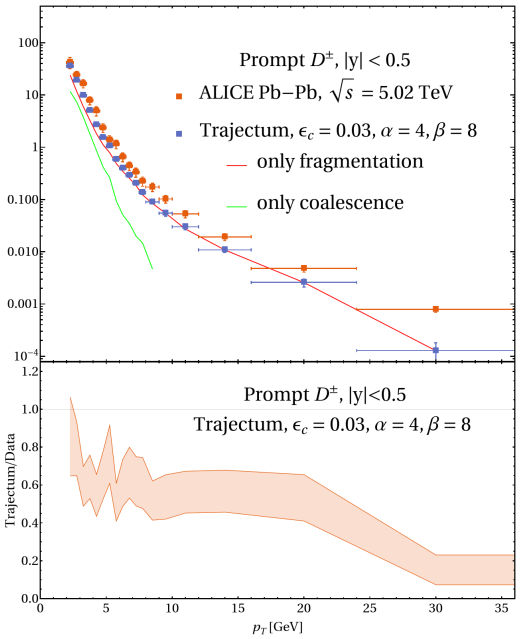

Figure 26: $D^{\pm}$ p_{T}-differential multiplicity with an explicit PDG = 411 selection compared to ALICE measurements [92].

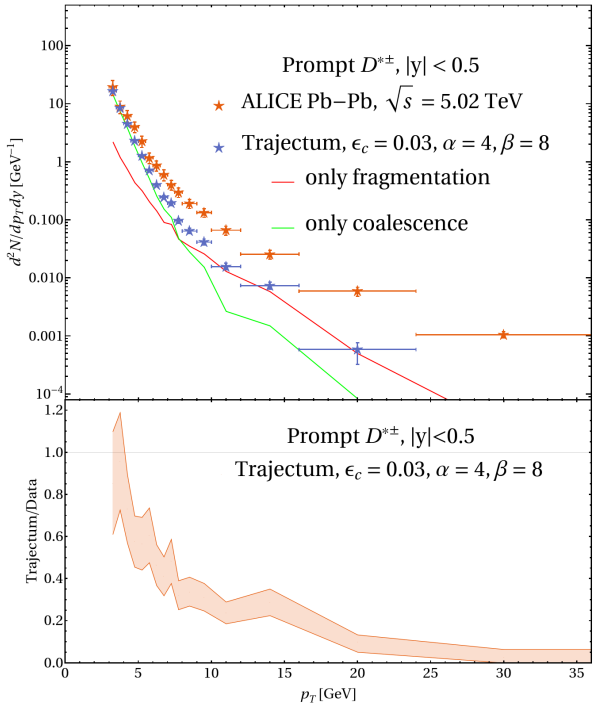

Figure 27: $D^{*\pm}$ p_{T}-differential multiplicity with an explicit PDG = 413 selection compared to ALICE measurements [92].

B Appendix

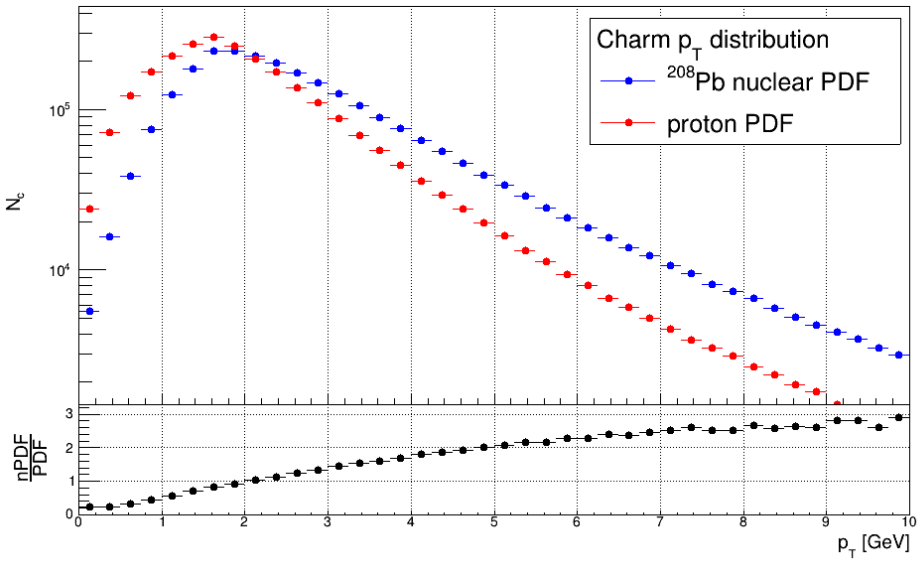

Figure 28: Ratio of the initial transverse momentum spectra for charm quarks between a nuclear ^{208}Pb PDF and a proton PDF.

References

[1] Miklos Gyulassy and Larry McLerran. New forms of qcd matter discovered at rhic. *Nuclear Physics A*, 750(1):30–63, 2005. Quark-Gluon Plasma. New Discoveries at RHIC: Case for the Strongly Interacting Quark-Gluon Plasma. Contributions from the RBRC Workshop held May 14-15, 2004.

[2] Wit Busza, Krishna Rajagopal, and Wilke van der Schee. Heavy Ion Collisions: The Big Picture, and the Big Questions. *Ann. Rev. Nucl. Part. Sci.*, 68:339–376, 2018.

[3] Xin Dong and Vincenzo Greco. Heavy quark production and properties of Quark–Gluon Plasma. *Prog. Part. Nucl. Phys.*, 104:97–141, 2019.

[4] Roman Pasechnik and Michal Šumbera. Phenomenological Review on Quark–Gluon Plasma: Concepts vs. Observations. *Universe*, 3(1):7, 2017.

[5] Ulrich Heinz and Raimond Snellings. Collective flow and viscosity in relativistic heavy-ion collisions. *Annual Review of Nuclear and Particle Science*, 63(1):123–151, October 2013.

[6] Lyndon Evans and Philip Bryant. Lhc machine. *Journal of Instrumentation*, 3(08):S08001, aug 2008.

[7] Li-juan Ruan. Relativistic heavy-ion collider (rhic) physics overview. *Frontiers of Physics in China*, 5(2):205–214, May 2010.

[8] Matteo Cacciari, Paolo Nason, and Ramona Vogt. Qcd predictions for charm and bottom quark production at rhic. *Phys. Rev. Lett.*, 95:122001, Sep 2005.

[9] Shuang Li, Chaowen Wang, Xianbao Yuan, and Shengqin Feng. Production of open-charm mesons in relativistic heavy-ion collisions. *Phys. Rev. C*, 98:014909, Jul 2018.

[10] R. Baier, Yu.L. Dokshitzer, A.H. Mueller, S. Peigné, and D. Schiff. Radiative energy loss and p_t-broadening of high energy partons in nuclei. *Nuclear Physics B*, 484(1):265–282, 1997.

[11] P Braun-Munzinger. Quarkonium production in ultra-relativistic nuclear collisions: suppression versus enhancement. *Journal of Physics G: Nuclear and Particle Physics*, 34(8):S471, jul 2007.

[12] A. et al. Andronic. Heavy-flavour and quarkonium production in the lhc era: from proton–proton to heavy-ion collisions. *The European Physical Journal C*, 76(3), February 2016.

[13] Xinye Peng. Non-strange and strange d-meson and charm-baryon production in heavy-ion collisions measured with alice at the lhc. *Nuclear Physics A*, 982:667–670, 2019. The 27th International Conference on Ultrarelativistic Nucleus-Nucleus Collisions: Quark Matter 2018.

[14] S. et al. Acharya. Measurement of $\mathrm{D}^0, \mathrm{D}^+, \mathrm{D}^{*+}$ and D_s^+ production in pp collisions at $\sqrt{s} = 5.02$ TeV with ALICE. *The European Physical Journal C*, 79(5), May 2019.

[15] Guang-You Qin, Hannah Petersen, Steffen A. Bass, and Berndt Müller. Translation of collision geometry fluctuations into momentum anisotropies in relativistic heavy-ion collisions. *Phys. Rev. C*, 82:064903, Dec 2010.

[16] S. Voloshin and Y. Zhang. Flow study in relativistic nuclear collisions by fourier expansion of azimuthal particle distributions. *Zeitschrift fur Physik C Particles and Fields*, 70(4):665–671, May 1996.

[17] A. M. Poskanzer and S. A. Voloshin. Methods for analyzing anisotropic flow in relativistic nuclear collisions. *Phys. Rev. C*, 58:1671–1678, Sep 1998.

[18] Sooraj Radhakrishnan. Measurements of open charm production in au+au collisions at snn=200gev with the star experiment at rhic. *Nuclear Physics A*, 982:659–662, 2019. The 27th International Conference on Ultrarelativistic Nucleus-Nucleus Collisions: Quark Matter 2018.

[19] B. A. Kniehl, G. Kramer, I. Schienbein, and H. Spiesberger. Collinear subtractions in hadroproduction of heavy quarks. *The European Physical Journal C*, 41(2):199–212, May 2005.

[20] Bernd A. Kniehl, Gustav Kramer, Ingo Schienbein, and Hubert Spiesberger. Inclusive charmed-meson production at the cern lhc. *The European Physical Journal C*, 72(7), July 2012.

[21] S. Plumari, V. Minissale, S. K. Das, G. Coci, and V. Greco. Charmed hadrons from coalescence plus fragmentation in relativistic nucleus-nucleus collisions at rhic and lhc. *The European Physical Journal C*, 78(4), April 2018.

[22] Hai-hong Li, Feng-lan Shao, Jun Song, and Rui-qin Wang. Production of single-charm hadrons by the quark-combination mechanism in p-pb collisions at $\sqrt{s_{NN}} = 5.02$ tev. *Physical Review C*, 97(6), June 2018.

[23] Govert Hugo Nijs. *Holography in Quark-Gluon Plasma and Neutron Stars*. PhD thesis, Utrecht University, 2020.

[24] Govert Nijs, Wilke van der Schee, Umut Gürsoy, and Raimond Snellings. Bayesian analysis of heavy ion collisions with the heavy ion computational framework trajectum. *Physical Review C*, 103(5), May 2021.

[25] Wikipedia. Standard model visualisation, 2004. [Online; accessed 22-July-2004].

[26] Mark Thomson. *Modern particle physics*. Cambridge University Press, New York, 2013.

[27] G.M. Prosperi, M. Raciti, and C. Simolo. On the running coupling constant in qcd. *Progress in Particle and Nuclear Physics*, 58(2):387–438, 2007.

[28] A. K. Chaudhuri. A short course on relativistic heavy ion collisions, 2012.

[29] Rajan Gupta. Introduction to lattice qcd, 1998.

[30] Claudia Ratti. Lattice qcd and heavy ion collisions: a review of recent progress. *Reports on Progress in Physics*, 81(8):084301, July 2018.

[31] S. Muroya, A. Nakamura, C. Nonaka, and T. Takaishi. Lattice qcd at finite density: An introductory review. *Progress of Theoretical Physics*, 110(4):615–668, October 2003.

[32] Nora Brambilla, Antonio Pineda, Joan Soto, and Antonio Vairo. Potential nrqcd: an effective theory for heavy quarkonium. *Nuclear Physics B*, 566(1–2):275–310, January 2000.

[33] C.P. Burgess. An introduction to effective field theory. *Annual Review of Nuclear and Particle Science*, 57(1):329–362, November 2007.

[34] L.D. LANDAU and E.M. LIFSHITZ. Chapter xv - relativistic fluid dynamics. In L.D. LANDAU and E.M. LIFSHITZ, editors, *Fluid Mechanics (Second Edition)*, pages 505–514. Pergamon, second edition edition, 1987.

[35] PAUL ROMATSCHKE. New developments in relativistic viscous hydrodynamics. *International Journal of Modern Physics E*, 19(01):1–53, January 2010.

[36] Werner Israel and John M Stewart. Transient relativistic thermodynamics and kinetic theory. *Annals of Physics*, 118(2):341–372, 1979.

[37] ALICE Collaboration. The alice experiment – a journey through qcd, 2022.

[38] Xin Dong and Vincenzo Greco. Heavy quark production and properties of quark–gluon plasma. *Progress in Particle and Nuclear Physics*, 104:97–141, 2019.

[39] Aleksi Kurkela and Yan Zhu. Isotropization and hydrodynamization in weakly coupled heavy-ion collisions. *Physical Review Letters*, 115(18), October 2015.

[40] Wilke van der Schee, Paul Romatschke, and Scott Pratt. Fully dynamical simulation of central nuclear collisions. *Physical Review Letters*, 111(22), November 2013.

[41] Jonah E. Bernhard. Bayesian parameter estimation for relativistic heavy-ion collisions, 2018.

[42] Guy D. Moore and Derek Teaney. How much do heavy quarks thermalize in a heavy ion collision? *Phys. Rev. C*, 71:064904, Jun 2005.

[43] Guang-You Qin, Jörg Ruppert, Charles Gale, Sangyong Jeon, and Guy D. Moore. Jet energy loss, photon production, and photon-hadron correlations at energies available at the bnl relativistic heavy ion collider (rhic). *Phys. Rev. C*, 80:054909, Nov 2009.

[44] Yu.L Dokshitzer and D.E Kharzeev. Heavy-quark colorimetry of qcd matter. *Physics Letters B*, 519(3):199–206, 2001.

[45] Shanshan Cao, Guang-You Qin, and Steffen A. Bass. Heavy-quark dynamics and hadronization in ultrarelativistic heavy-ion collisions: Collisional versus radiative energy loss. *Physical Review C*, 88(4), October 2013.

[46] Shanshan Cao and Steffen A. Bass. Thermalization of charm quarks in infinite and finite quark-gluon plasma matter. *Physical Review C*, 84(6), December 2011.

[47] Francesco Prino and Ralf Rapp. Open heavy flavor in qcd matter and in nuclear collisions. *Journal of Physics G: Nuclear and Particle Physics*, 43(9):093002, August 2016.

[48] H.-T. Ding, A. Francis, O. Kaczmarek, F. Karsch, H. Satz, and W. Soeldner. Charmonium properties in hot quenched lattice qcd. *Physical Review D*, 86(1), July 2012.

[49] Debasish Banerjee, Saumen Datta, Rajiv Gavai, and Pushan Majumdar. Heavy quark momentum diffusion coefficient from lattice qcd. *Physical Review D*, 85(1), January 2012.

[50] K. Huggins and R. Rapp. A t-matrix calculation for in-medium heavy-quark gluon scattering. *Nuclear Physics A*, 896:24–45, December 2012.

[51] F. Riek and R. Rapp. Quarkonia and heavy-quark relaxation times in the quark-gluon plasma. *Physical Review C*, 82(3), September 2010.

[52] Benjamin Svetitsky. Diffusion of charmed quarks in the quark-gluon plasma. *Phys. Rev. D*, 37:2484–2491, May 1988.

[53] Yasuyuki Akiba, Aaron Angerami, Helen Caines, Anthony Frawley, Ulrich Heinz, Barbara Jacak, Jiangyong Jia, Tuomas Lappi, Wei Li, Abhijit Majumder, David Morrison, Mateusz Ploskon, Joern Putschke, Krishna Rajagopal, Ralf Rapp, Gunther Roland, Paul Sorensen, Urs Wiedemann, Nu Xu, and W. A. Zajc. The hot qcd white paper: Exploring the phases of qcd at rhic and the lhc, 2015.

[54] Matteo Cacciari and Einan Gardi. Heavy-quark fragmentation. *Nuclear Physics B*, 664(1–2):299–340, August 2003.

[55] J. D. Bjorken. Properties of hadron distributions in reactions containing very heavy quarks. *Phys. Rev. D*, 17:171–173, Jan 1978.

[56] C. Peterson, D. Schlatter, I. Schmitt, and P. M. Zerwas. Scaling violations in inclusive e^+e^- annihilation spectra. *Phys. Rev. D*, 27:105–111, Jan 1983.

[57] V.G. Kartvelishvili, A.K. Likhoded, and V.A. Petrov. On the fragmentation functions of heavy quarks into hadrons. *Physics Letters B*, 78(5):615–617, 1978.

[58] P D B Collins and T P Spiller. The fragmentation of heavy quarks. *Journal of Physics G: Nuclear Physics*, 11(12):1289, dec 1985.

[59] M. G. Bowler. e+ e- Production of Heavy Quarks in the String Model. *Z. Phys. C*, 11:169, 1981.

[60] Xin Dong. Heavy flavor production, energy loss and flow — experimental overview. *Nuclear Physics A*, 967:192–199, 2017. The 26th International Conference on Ultra-relativistic Nucleus-Nucleus Collisions: Quark Matter 2017.

[61] Vincenzo Minissale, Salvatore Plumari, and Vincenzo Greco. Charm hadrons in pp collisions at lhc energy within a coalescence plus fragmentation approach. *Physics Letters B*, 821:136622, 2021.

[62] Yongseok Oh, Che Ming Ko, Su Houng Lee, and Shigehiro Yasui. Ratios of heavy baryons to heavy mesons in relativistic nucleus-nucleus collisions. *Phys. Rev. C*, 79:044905, Apr 2009.

[63] S Bass. Microscopic models for ultrarelativistic heavy ion collisions. *Progress in Particle and Nuclear Physics*, 41:255–369, 1998.

[64] Hannah Petersen, Dmytro Oliinychenko, Markus Mayer, Jan Staudenmaier, and Sangwook Ryu. Smash – a new hadronic transport approach. *Nuclear Physics A*, 982:399–402, February 2019.

[65] Michael L. Miller, Klaus Reygers, Stephen J. Sanders, and Peter Steinberg. Glauber modeling in high-energy nuclear collisions. *Annual Review of Nuclear and Particle Science*, 57(1):205–243, November 2007.

[66] Michał Barej, Adam Bzdak, and Paweł Gutowski. Wounded-quark emission function at the top energy available at the bnl relativistic heavy ion collider. *Physical Review C*, 97(3), March 2018.

[67] C. Loizides. Glauber modeling of high-energy nuclear collisions at the subnucleon level. *Physical Review C*, 94(2), August 2016.

[68] Piotr Bożek, Wojciech Broniowski, and Maciej Rybczyński. Wounded quarks in collisions. *Physical Review C*, 94(1), July 2016.

[69] Kevin Welsh, Jordan Singer, and Ulrich Heinz. Initial-state fluctuations in collisions between light and heavy ions. *Physical Review C*, 94(2), August 2016.

[70] Ryan D. Weller and Paul Romatschke. One fluid to rule them all: Viscous hydrodynamic description of event-by-event central p+p, p+pb and pb+pb collisions at 5.02 tev. *Physics Letters B*, 774:351–356, November 2017.

[71] J. Scott Moreland, Jonah E. Bernhard, and Steffen A. Bass. Alternative ansatz to wounded nucleon and binary collision scaling in high-energy nuclear collisions. *Physical Review C*, 92(1), July 2015.

[72] Steven S. Gubser. Symmetry constraints on generalizations of bjorken flow. *Physical Review D*, 82(8), October 2010.

[73] Steven S. Gubser and Amos Yarom. Conformal hydrodynamics in minkowski and de sitter spacetimes. *Nuclear Physics B*, 846(3):469–511, May 2011.

[74] Hugo Marrochio, Jorge Noronha, Gabriel S. Denicol, Matthew Luzum, Sangyong Jeon, and Charles Gale. Solutions of conformal israel-stewart relativistic viscous fluid dynamics. *Physical Review C*, 91(1), January 2015.

[75] C. Loizides, J. Nagle, and P. Steinberg. Improved version of the phobos glauber monte carlo. *SoftwareX*, 1–2:13–18, September 2015.

[76] M. Sievert and J. Noronha-Hostler. Cern large hadron collider system size scan predictions for pbpb, xexe, arar, and oo with relativistic hydrodynamics. *Physical Review C*, 100(2), August 2019.

[77] Constantin Loizides, Jason Kamin, and David d'Enterria. Improved monte carlo glauber predictions at present and future nuclear colliders. *Phys. Rev. C*, 97:054910, May 2018.

[78] A. et al. Bazavov. Equation of state in (2+1)-flavor qcd. *Physical Review D*, 90(9), November 2014.

[79] G. S. Denicol, S. Jeon, and C. Gale. Transport coefficients of bulk viscous pressure in the 14-moment approximation. *Physical Review C*, 90(2), August 2014.

[80] Fred Cooper and Graham Frye. Single-particle distribution in the hydrodynamic and statistical thermodynamic models of multiparticle production. *Phys. Rev. D*, 10:186–189, Jul 1974.

[81] Christian Bierlich, Smita Chakraborty, Nishita Desai, Leif Gellersen, Ilkka Helenius, Philip Ilten, Leif Lönnblad, Stephen Mrenna, Stefan Prestel, Christian T. Preuss, Torbjörn Sjöstrand, Peter Skands, Marius Utheim, and Rob Verheyen. A comprehensive guide to the physics and usage of pythia 8.3, 2022.

[82] Andy Buckley, James Ferrando, Stephen Lloyd, Karl Nordström, Ben Page, Martin Rüfenacht, Marek Schönherr, and Graeme Watt. Lhapdf6: parton density access in the lhc precision era. *The European Physical Journal C*, 75(3), March 2015.

[83] Richard D. Ball, Valerio Bertone, Stefano Carrazza, Luigi Del Debbio, Stefano Forte, Alberto Guffanti, Nathan P. Hartland, and Juan Rojo. Parton distributions with qed corrections. *Nuclear Physics B*, 877(2):290–320, December 2013.

[84] S. et al. Acharya. Charm-quark fragmentation fractions and production cross section at midrapidity in pp collisions at the lhc. *Physical Review D*, 105(1), January 2022.

[85] et al. O. Biebel. Fragmentation functions in e^+e^-, ep and pp collisions, 2017.

[86] Shuang Li and Jinfeng Liao. Data-driven extraction of heavy quark diffusion in quark-gluon plasma. *The European Physical Journal C*, 80(7), July 2020.

[87] G. E. P. Box and Mervin E. Muller. A Note on the Generation of Random Normal Deviates. *The Annals of Mathematical Statistics*, 29(2):610 – 611, 1958.

[88] Kari J. Eskola, Petja Paakkinen, Hannu Paukkunen, and Carlos A. Salgado. Epps16: nuclear parton distributions with lhc data. *The European Physical Journal C*, 77(3), March 2017.

[89] S. et al. Acharya. d-meson azimuthal anisotropy in midcentral pb-pb collisions at $\sqrt{s}_{nn}$ = 5.02 TeV. *Phys. Rev. Lett.*, 120:102301, Mar 2018.

[90] S. et al. Acharya. Transverse-momentum and event-shape dependence of d-meson flow harmonics in pb–pb collisions at $\sqrt{s_{NN}} = 5.02$ TeV. *Physics Letters B*, 813:136054, February 2021.

[91] Shreyasi Acharya et al. First measurement of $\Lambda_c^{\pm}$ production down to $p_T = 0$ in pp and p-Pb collisions at $\sqrt{s_{NN}} = 5.02$ TeV. year, 2023.

[92] S. et al. Acharya. Prompt $D^0, D^+ and D^{*+}$ production in Pb-Pb collisions at $\sqrt{s} = 5.02$ TeV. *Journal of High Energy Physics*, 174(5), january 2022.

[93] Ben-Wei Zhang, Enke Wang, and Xin-Nian Wang. Heavy quark energy loss in a nuclear medium. *Phys. Rev. Lett.*, 93:072301, Aug 2004.